N70-20490

NASA-CR-108917

Final Report

ANALYSIS OF HOLOGRAMS of REACTING SPRAYS

R. F. WUERKER, B. J. MATTHEWS, B. J. HECKERT

TRW SYSTEMS GROUP
ONE SPACE PARK, REDONDO BEACH, CALIFORNIA

TRW REPORT NO. 12299-6001-R0-00
JANUARY 1970

JPL CONTRACT NO. 952357

JET PROPULSION LABORATORY
CALIFORNIA INSTITUTE OF TECHNOLOGY
PASADENA, CALIFORNIA

Final Report

ANALYSIS OF HOLOGRAMS of REACTING SPRAYS

R. F. WUERKER, B. J. MATTHEWS, B. J. HECKERT

TRW SYSTEMS GROUP
ONE SPACE PARK, REDONDO BEACH, CALIFORNIA

TRW REPORT NO. 12299-6001-R0-00
JANUARY 1970

JPL CONTRACT NO. 952357

"THIS WORK WAS PERFORMED FOR THE JET PROPULSION LABORATORY, CALIFORNIA INSTITITE OF TECHNOLOGY, AS SPONSORED BY THE NATIONAL AERONAUTICS AND SPACE ADMINISTRATION UNDER CONTRACT NAS7-100"

FOREWORD

This is the final report on the "Analysis of Holograms of Reacting Sprays" contract sponsored by the Jet Propulsion Laboratory, California Institute of Technology, Pasadena, California. The report is submitted by TRW Systems Group, TRW, Inc., in accordance with the provisions of JPL Contract Number 9252357. The holograms analyzed during the current effort were recorded as part of the work under a previous JPL sponsored program: "Producing Holograms of Reacting Sprays in Liquid Propellant Rocket Engines," Contract Number 952023. Analysis of these holograms under the current contract was a logical outgrowth of the earlier work. This work was accomplished by the Science and Technology Division of TRW Systems Group. The Project Manager was Mr. B. J. Matthews. Dr. R. F. Wuerker served as the Principal Scientist. The contract was administered technically by Messrs. R. M. Clayton and R. S. Rogero of the Jet Propulsion Laboratory.

Work presented in this final report is based upon the efforts and contributions of the following TRW personnel: R. A. Briones, S. S. Cherry, R. J. Chouinard, M. S. Jennings, M. von Moltke, M. S. Sendro and P. B. Verenkoff. The hologram of a reacting spray in a windowed combustion chamber used for data reduction purposes was recorded during a companion holography program sponsored by the Air Force (Contract F04611-69-C-0015). Permission to utilize this hologram was through the courtesy of Lt. W. B. Kuykendal, Air Force Rocket Propulsion Laboratory, Edwards Air Force Base.

ABSTRACT

Holograms of reacting and non-reacting droplet sprays, recorded during a previous contract for the Jet Propulsion Laboratory, were reconstructed and photographed for the purpose of evaluation and data reduction. The virtual image reconstruction was accomplished with a pulsed ruby laser and the reference beam optics of the holocamera originally used to record the hologram. A 4- by 5-inch view camera, focused on a preselected plane of interest in the scene volume, photographed the reconstruction on very fine grain film emulsion. These negatives, together with positive prints of the negatives, were subjected to manual drop size measurements. Drop size data were analyzed and correlations made with empirical mean droplet diameters. Size distributions of the measured droplets were also compared with published experimental data from the literature. Precise holocamera resolution measurements were made using the same recording-reconstruction techniques described for the droplet sprays. These measurements served to help define the smallest droplets which could be resolved and, further, to indicate the effect on resolution of coherent light granularity.

Table of Contents

Page

LIST OF ILLUSTRATIONS

LIST OF ILLUSTRATIONS (Continued)

LIST OF ILLUSTRATIONS (Continued)

1. INTRODUCTION

The feasibility of holographically recording liquid propellant combustion phenomena was first demonstrated in 1968 during a previous research program sponsored by the Jet Propulsion Laboratory.* The pulsed ruby laser holocamera apparatus, liquid rocket engine test hardware, test procedures and holographic results of this earlier work have been reported in the literature.[1, 2, 3, 4] At that time, all efforts were directed toward developing adequate techniques for making holograms of reacting sprays. As a consequence, there was no systematic attempt at acquiring quantitative data from the reconstructions of burning liquid propellants. Only qualitative impressions were noted. Ultimately, the utility of holographic methods for studying combusting sprays is strongly dependent upon deriving quantitative information from the reconstructions which could then be used to describe or model the combustion process.

The work reported here is a logical extension of the initial holography program. Holograms recorded during the previous effort were reviewed for general quality and information content. Twelve holograms were initially selected for further study. The purpose of this study was to evaluate and analyze several of the best reconstructions for both qualitative and quantitative information concerning the spray phenomena. The acquisition and analysis of droplet data was preceded by systematic 1) resolution measurements with the JPL 45-degree transmission holocamera and pulsed ruby laser apparatus, and 2) development of improved image reconstruction techniques to facilitate drop size measurements. The following sections of this final report present the experimental techniques used and discuss the data derived from the holograms.

---

* JPL Contract No. 952023 (NAS7-100), "Producing Holograms of Reacting Sprays in Liquid Propellant Rocket Engines."

2. TECHNICAL DISCUSSION

2.1 GENERAL

Final evaluation of the spray holograms is, in part, dependent upon the resolving power of the entire optical system used to record, reconstruct and subsequently photocopy the reconstructed image. Resolution of the JPL 45-degree holocamera had not been precisely determined during the earlier work. This was accomplished during the first part of the program together with development of an improved method for precise ruby hologram reconstruction. The reconstructed holograms were photographically copied using a high quality camera lens and fine grain film. Sections 2.2 and 2.3 describe this work and the measured resolving power of the holocamera apparatus together with the effect on resolution of coherent light granularity phenomena.

Succeeding text (Sections 2.4 through 3.6) is concerned with the technique used to reduce droplet data, resulting experimental information and a discussion of the results. In the latter section, experimental results are correlated with accepted mean droplet diameter and droplet size distributions. An assessment of droplet measurement error is also presented. Finally, the feasibility of using holographically recorded reacting spray droplet data for combustion modeling is briefly described and demonstrated in Section 3.3 in a preliminary manner.

2.2 JPL HOLOCAMERA RESOLUTION

Resolution of the JPL 45-degree transmission holocamera (Figure 1) was determined experimentally using a U. S. Air Force 1951 resolution target.* A photograph of the USAF 1951 resolution target is shown in Figure 2. The target was placed within the scene volume of the ruby laser holocamera and holographed. A schematic diagram of the test setup is presented in Figure 3. Resolution measurements were made at distances of 94 centimeters (37 inches), 45 centimeters (~18 inches) and 25 centimeters (10 inches) from the holographic film plate to the resolution target. The later two distances were chosen to approximately correspond with the center

---

*USAF 1951 Resolving Power Target per Military Standard 150A, Cat. No. 8040, W. & L. E. Gurley, Troy, New York.

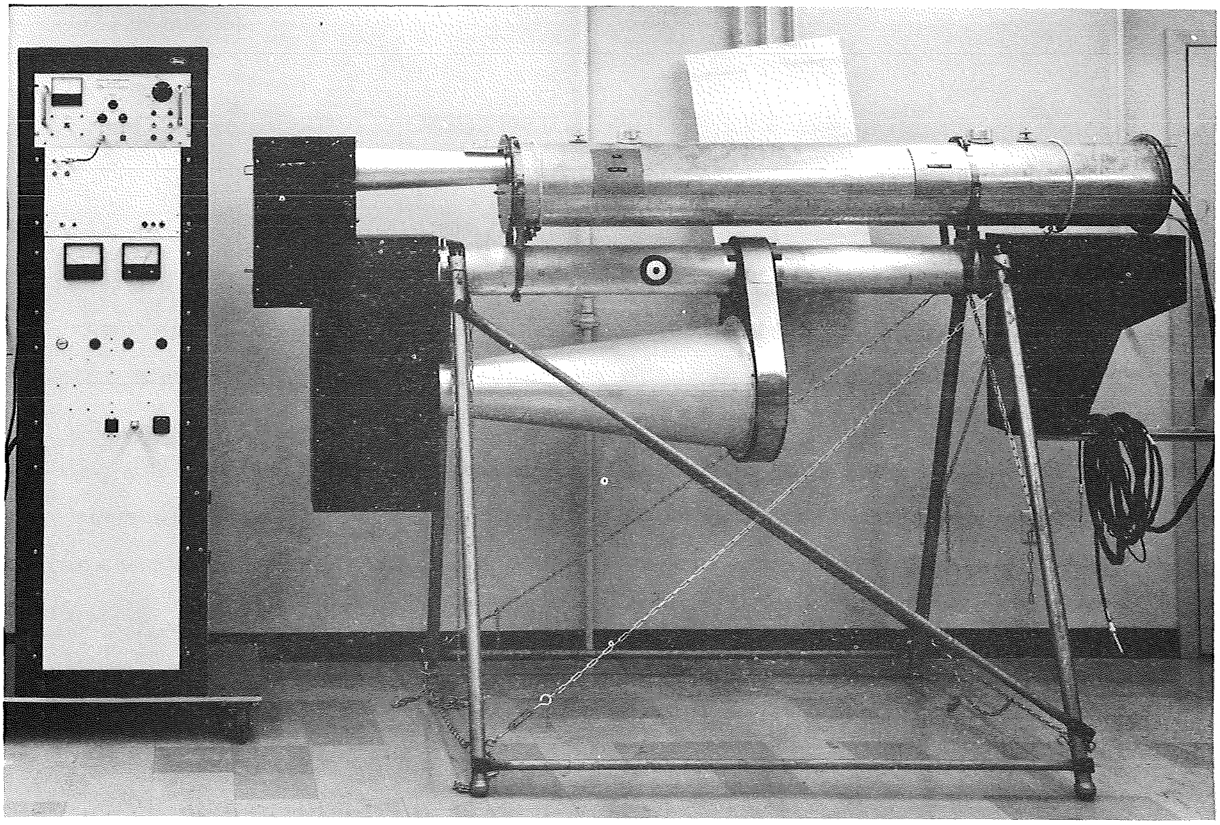

Figure 1. JPL 45-degree Two-beam Transmission Holocamera

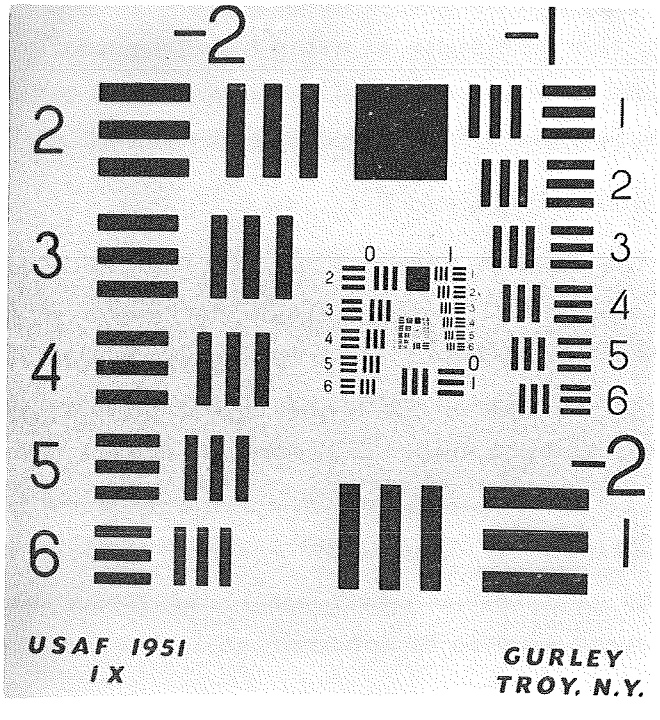

Figure 2. U.S. Air Force 1951 Resolving Power Test Target

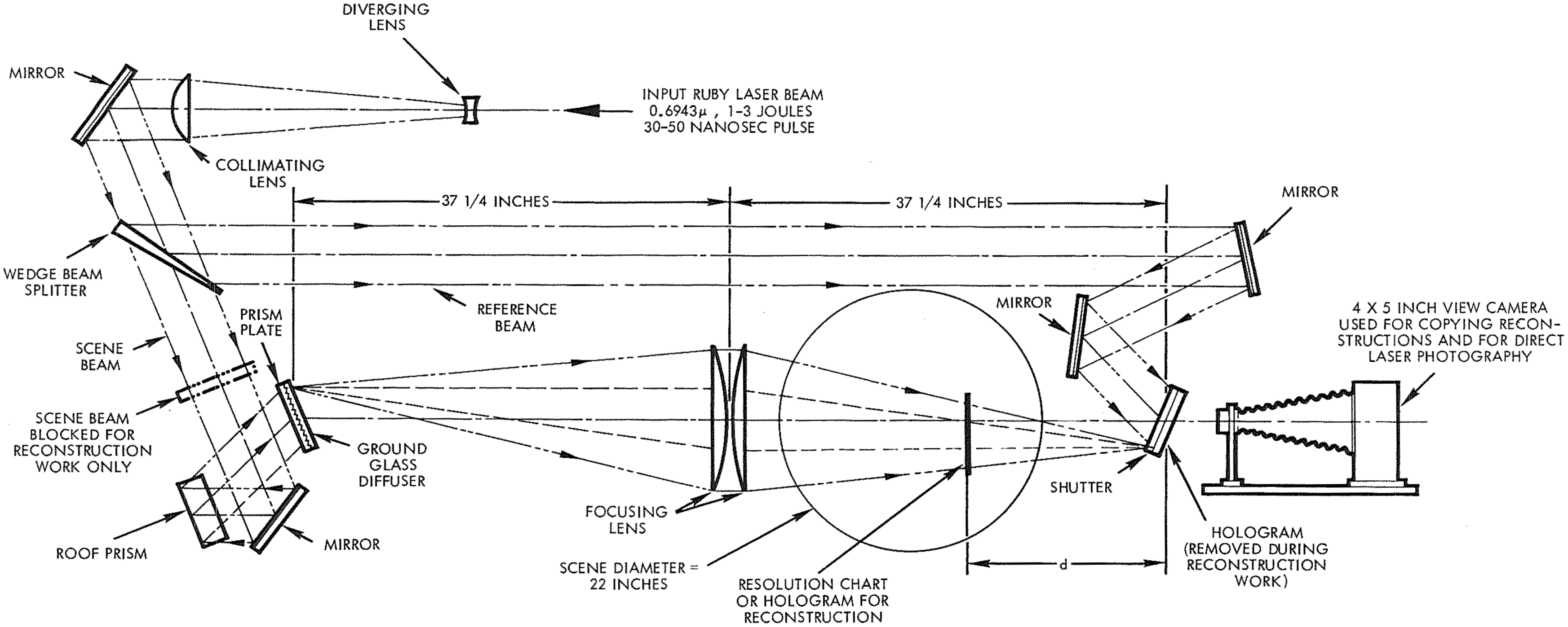

Figure 3. Schematic of Holocamera Test Setup for Hologram Reconstruction and Photocopying

of the atmospheric reacting spray fan and the 3-inch-diameter combustion chamber locations within the holocamera scene volume during the original holographic test program at the JPL Edwards Test Site.

At a distance of 45 centimeters from the film plate to the target, the holocamera resolution was determined to be 20 line pairs per millimeter. This corresponds to an equivalent partical size resolution of ~25 microns.[5]

Verification of this statement on resolution is presented in Figures 4 and 5. These figures show photographic enlargements of a portion of the USAF 1951 target. Figure 4 is an intermediate enlargement of the three photographs, while Figure 5 represents a maximum magnification of the same three images. In each case, the original photographs were made using SO-243 film[*] with a 4 by 5-inch bellows view camera and a Schneider Kreuznach Component 1:5.6/300 millimeter lens.

The left-hand picture (Figures 4 and 5) was made with the resolution target located in the holocamera scene volume and using white incoherent rear illumination. The target was photographed with the copy camera lens and film combination previously noted. The camera lens-resolution target distance (i.e., object distance) was approximately 50 centimeters (~19.7 inches). Using a microscope, the negative for the left-hand picture was "read" to a resolution of 80 line pairs per millimeter (equivalent to about 6 micron partical size).[**]

---

[*] Product of Eastman Kodak Co., Rochester, N. Y. The SO-243 Special High Definition Aerial Film is a panchromatic emulsion with extended red sensitivity and a resolving power in excess of 200 lines per millimeter. (Refer to Kodak Publication No. M-118-0, Section 19). When the lefthand photograph of Figure 4 (Figure 5 is the same) was examined with a microscope, the negative exhibited a grain size just resolvable at a 125 power magnification (~1 micron).

[**] Appendix A provides a description of the USAF 1951 chart and listing of the bar or line pair spacings.

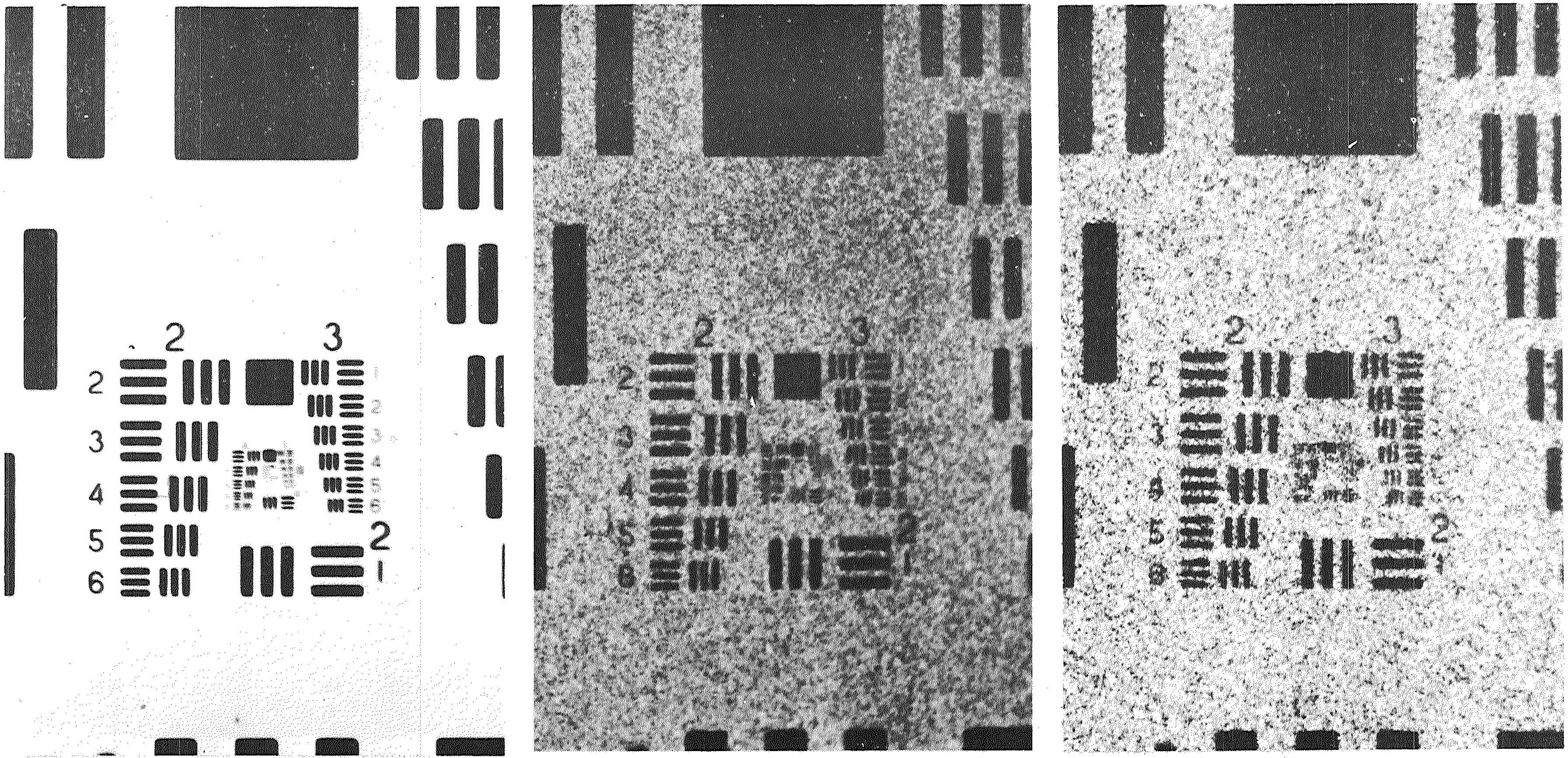

Figure 4. Copies of three photographs of USAF 1951 resolution chart taken with white incoherent rear illumination (left picture), with ruby laser coherent illumination (center picture), and of the ruby laser reconstruction of a ruby laser hologram (right picture). All three were made under identical conditions of illumination as the center photograph. The pictures were recorded with a 4- by 5-inch bellows copy camera with Schneider Kreuznach 1:5.6/300 mm lens, using Eastman S0243 film. The photographs were recorded with the chart mounted within the scene volume of the JPL ruby laser holocamera.

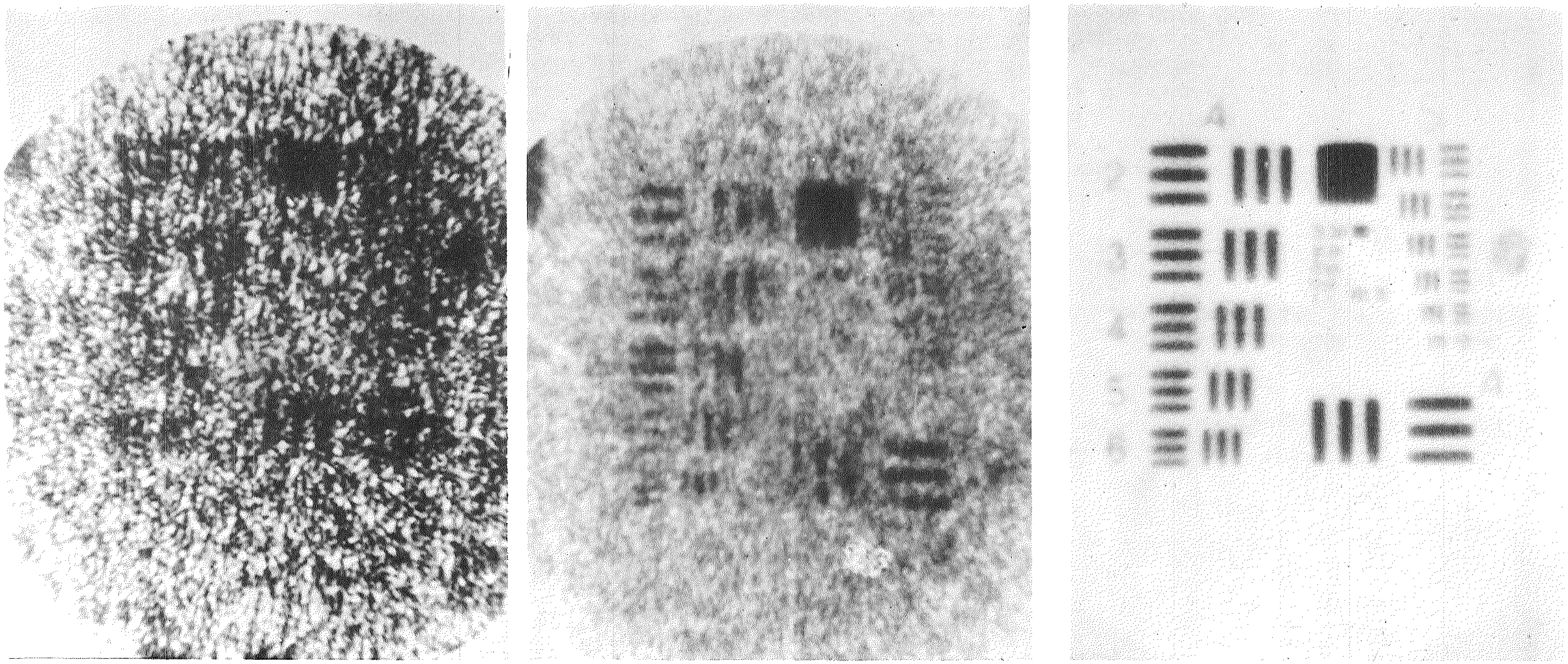

Figure 5. Copies of three photomicrographs of three S0243 negatives taken in the "JPL holocamera" with white light illumination (left picture), direct ruby light coherent illumination (center picture), and of a ruby laser reconstruction (right picture) of a ruby laser hologram made in the same holocamera. All three negatives were taken under identical conditions. The three original negatives were recorded with a Schneider Kreuznach 1:5. 6/300 mm lens. The resolution chart was mounted in the scene volume of the holocamera at 45 centimeters distance from the hologram. Resolution of the left picture is 6-3 (80 line pairs per millimeter); resolution of the center picture is 5-3 (40 line pairs per millimeter); and resolution of the right picture is 4-1 (18 line pairs per millimeter).

The center photograph shown in Figure 4 and further enlarged in Figure 5 was made under identical conditions to the white light photograph except that the USAF 1951 target was illuminated with coherent red light (λ = 0.6943 micron) from a pulsed ruby laser. The background is now granular, due to the use of coherent light. Examination of this negative showed that it could be read to the 5th column, 3rd row, or 40 line pairs per millimeter.* The two photographs test the resolution of the holocamera for incoherent and red coherent light. The "factor-of-two" difference seems to be a rule which has been seen before.

The right hand picture in Figures 4 and 5 is of the reconstruction of a hologram of the resolution target taken under the identical conditions that the other two photographs were made. The hologram was recorded (on Agfa 8E75 plate) and reconstructed in the same holocamera. The hologram-resolution chart distance was 45 centimeters (~18 inches). This distance was about the same as the original Phase I open flame and the Phase II acrylic engine tests (see Reference 1). The hologram was reconstructed in the holocamera by blocking the scene beam and using the reference beam (see Figure 3) to reconstruct the virtual image. Thus, it was reconstructed with the identical reference beam pattern, reference beam angle, and wave length as it was recorded. The copy camera was not disturbed or changed between the recording of the real (center) and "synthetic" (right) images. The photograph was recorded on SO-243 film. Examination of the negative under a microscope showed it could read to 20 line pairs per millimeter.** The results in Figures 4 and 5 show that the hologram reconstruction is also limited by granularity, and that the hologram reconstruction is within a factor of 2 of a direct photograph. With even more work, this difference could be decreased.

In a procedure similar to that just described, resolution of the JPL holocamera at an object distance of 28 centimeters (~11 inches) was measured and again found to be ~20 line pairs per millimeter or about

---

*Examination of the negative with a 125X microscope showed that the granularity was 15 microns in size.

**Examination of the negative showed that the granularity size, on the average, was 20 microns in size.

25 microns in equivalent particle size. At a distance of 94 centimeters (~37 inches) resolution was 10 lines/millimeter or 50 microns.

A limiting factor in discerning fine detail in the reconstruction of any pulsed ruby hologram is the granular background which one observes when viewing the hologram. In discussing the resolution of the holocamera, some comments on laser granularity are appropriate here.

The "speckle" or granularity pattern which one observes when viewing laser-illuminated diffuse objects is a result of the high spacial coherence of the light from a laser. Granularity is not a by-product of holography. Rather, it is the inverse situation; namely, that the hologram in recreating a scene wave front, reproduces the granularity originally present. In actuality, the granularity is modified.

One way to understand this phenomenon is to consider a diffuse surface (such as a painted wall) illuminated by an enlarged collimated beam from a laser. The beam, in striking the diffuse surface, is scattered, but scattered coherently. This means that the phase of one spot is related by a constant multiple to the phase of a neighboring spot. This relationship holds all across the diffuse surface and is independent of time.

In observing the spot with the eye, each element of the surface is imaged on the retina of the eye. The intensity at the eye of a given element is the sum of all the rays traveling from the object to the image via the lens. This sum can either be maximum valued, or can be zero valued. The former corresponds to constructive interference of the component rays. The latter is due to destructive interference. The granularity, as will be seen, is a complex interference pattern whose spacing is determined by the diffraction resolution limit of the eye. The adjacent dark regions of destructive interference are separated one from another by an amount

$$\Delta \simeq \frac{2.44\, f\lambda}{D} , \qquad (1)$$

where D is the diameter of the lens, f is its focal length, and λ is the wavelength of laser light.

By decreasing the aperture (i. e., D), the granularity spacing increases. This can be seen by making a pinhole with the clenched index finger, and observing the diffuse spot with different pin hole sizes.

The same conditions hold for other optical imaging instruments, such as cameras, microscopes, telescopes, etc. For example, in looking into a microscope illuminated by laser light, the field appears granular. The higher the numerical value of the object, the smaller the granularity. Also, the higher the quality of the objective, the more random is the pattern. As with the eye, the granularity is spaced by the resolution limit. When examining small distributed phenomena, granularity can be most frustrating.

Cameras exhibit the same effect, namely, the developed film when examined shows the image superimposed by the random granularity pattern. Decreasing the aperture increases the spacing of the pattern. Increasing the aperture decreases the spacing. For this reason, it is best to photograph laser-illuminated scenes or hologram reconstructions with lenses of large aperture, small f number, even if the magnification is empty (inferior white light resolution of a large aperture lens).

Two photographs of a typical granularity pattern are shown in Figure 6. The examples were produced by illuminating an opal glass diffuser from behind with the beam from a helium-neon laser (Spectra Physics Model 124). A 1-millimeter-diameter aperture was placed before the illuminated spot to define its size. A polaroid film holder was placed 10 feet away from the 1-millimeter-diameter scatterer, and photographs were recorded on Polaroid film, Type 52, ASA 400. The examples seen in Figure 6 correspond to exposures of 10 and 2 seconds each. The two give a feeling for the intensity distribution of the maxima. For this arrangement, equation (1) gives the separation of the minima,

$$\Delta \approx \frac{2.44\, f\lambda}{D} = \frac{2.44\ (305\text{cm})(0.63\mu)}{0.1\ \text{cm}} = 0.47\ \text{cm} \quad .$$

Measurement of the recorded pattern verifies this prediction.

Decreasing the scatterer-photographic film distance decreases the separation of minima.

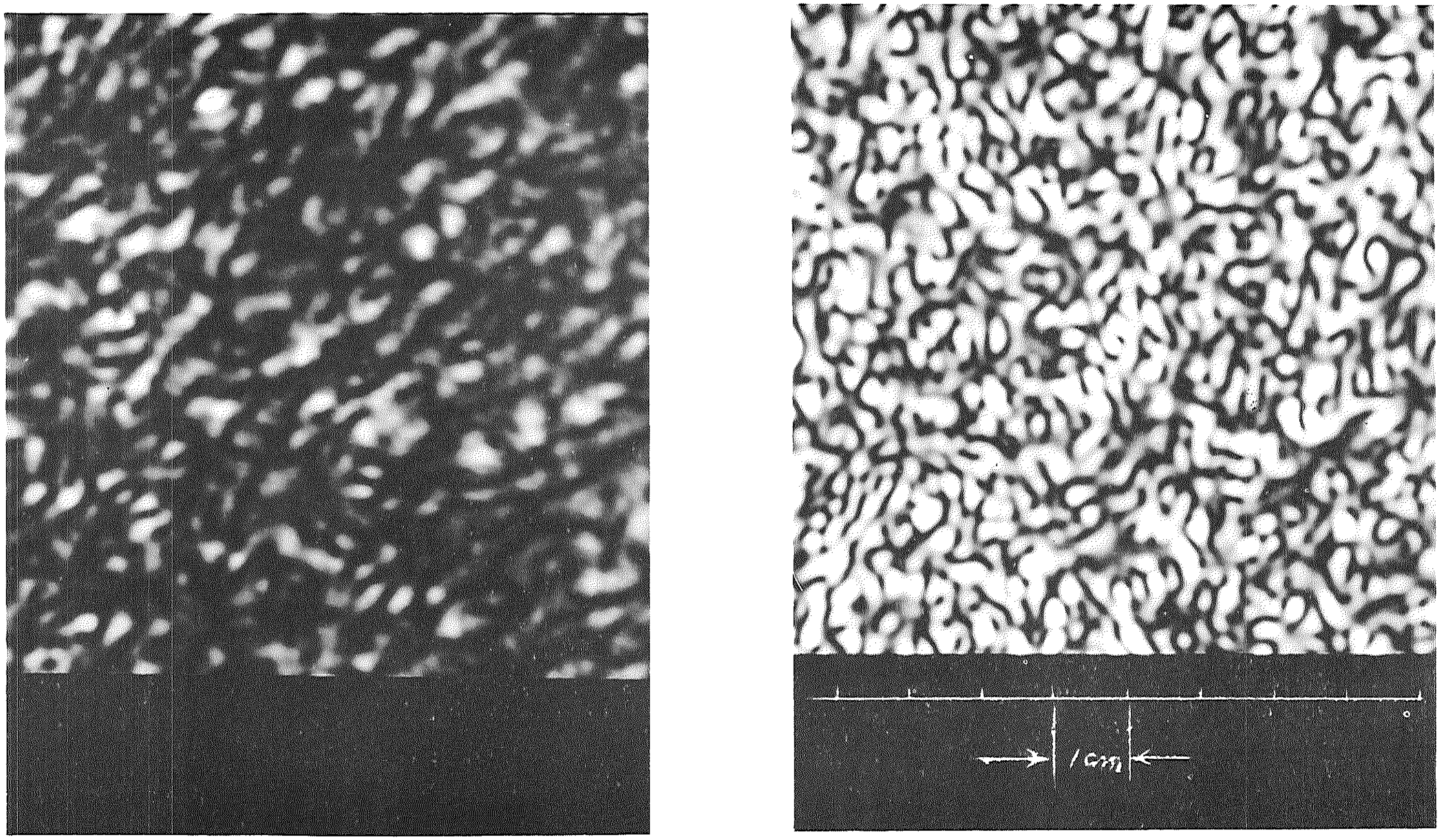

Figure 6. Photographs of a laser granularity pattern. The pattern was produced by illuminating an opal glass diffuser with the beam from a helium neon laser. The diffuse spot size was limited to a 1-millimeter diameter with an aperture. The resulting interference pattern was recorded at a distance of 10 feet (305 cm), on a piece of Polaroid film, Type 52 (ASA 400). Exposure time was 2 seconds for left-hand photo and 10 seconds for the right-hand photo.

Objects of the same size as the granularity such as reacting and nonreacting droplet sprays, hide in the granularity and are lost, particularly if the amount of light is low.

Granularity can be suppressed by moving the illuminating source during the observation time. In holography, this is impossible since such motions spoil the hologram recording. A method which is being investigated for decreasing the granularity of hologram reconstruction, without changing wavelength, includes multiple exposed holograms of the same scene. Each exposure is taken with a different reference beam angle, and the hologram is reconstructed serially.

2.3 DROPLET SPRAY HOLOGRAM RECONSTRUCTION

Twelve combustion holograms and one water spray hologram recorded during the previous contract were selected for preliminary review. Of the 13 holograms, 5 were recorded during the Phase I cold flow and open flame reacting spray tests (1 water spray fan and 4 open flame holograms. The remaining 8 holograms were from the Phase II experiments involving 3-inch-diameter acrylic combustion chambers. None were selected from the 18-inch-diameter Phase III tests. The preliminary selection of holograms is tabulated in Table I.

Reconstruction photographs of holograms of combustion phenomena were made using the technique developed during the resolution measurement tests described in Section 2.2. In this method, a hologram is replaced in the holocamera and reconstructed by illuminating it with the reference beam. When reconstructed in this manner, the reference beam is reproduced in wave length and divergence angle as when the holograms were recorded. The pattern, however, is not the same (as with the resolution holograms), since the ruby rods in the laser were changed between the time that the combustion holograms were recorded at JPL-ETS and the present work.

Each reacting and non-reacting spray hologram was placed in the film holder of the holocamera and a 4- x 5-inch view camera (lens at f/5.6) was focused on the virtual image space. The same magnification was maintained at each focal plane recorded in the scene volume. All pulsed ruby reconstruction photographs were recorded on Eastman SO-243 film.

Table I. Summary of Phase I and II Holograms Selected for Preliminary Evaluation

Run No.	Date	Viewing Station	Viewing Angle	P_{TO} psi	P_{TF} psi	W_o Lb/Sec	W_F Lb/Sec	O/F Ratio	Prop. Temp., °F		Remarks
									Oxid	Fuel	
B-1113W*	12-06-67	12 in. Downstream	Fan Plane	277	323	1.195	1.195	1.0			Water flow hologram.
1115Q*	1-15-68	Impingement Pt.	Fan Plane	220	593	1.203	1.529	0.786	56	58	Open flame: N_2O_4 and 50/50 N_2H_4 - UDMH.
1117G*	2-06-68	Impingement Pt.	Fan Plane	547	451	1.565	1.248	1.254	95	98	Open flame: N_2O_4 and 50/50 N_2H_4 - UDMH.
1115W*	1-17-68	Impingement Pt.	Fan Plane	407	382	1.605	1.163	1.380	53	52	Open flame: FNA-UDMH.
1115X*	1-17-68	Impingement Pt.	Fan Plane	641	254	2.035	0.943	2.158	53	56	Open flame: FNA-UDMH.
1149	4-25-68	Impingement Pt.	Fan Plane	391	455	0.509	0.400	1.272	50	46	3-Inch Chamber, N_2O_4 and 50/50 N_2H_4 - UDMH.
1154	4-26-68	Impingement Pt.	Fan Plane	401	452	0.502	0.396	1.268	103	106	3-Inch Chamber, N_2O_4 and 50/50 N_2H_4 - UDMH.
1156*	4-29-68	Impingement Pt.	Fan Plane	286	355	0.762	0.622	1.225	63	57	3-Inch Chamber, FNA-UDMH.
1157	4-29-68	Impingement Pt.	Fan Plane	434	371	0.517	0.330	1.566	35	40	3-Inch Chamber, FNA-UDMH.
1161*	4-30-68	Impingement Pt.	Fan Plane	300	320	0.808	0.570	1.417	105	110	3-Inch Chamber, FNA-UDMH.
1162	4-30-68	Impingement Pt.	Fan Plane	465	470	0.546	0.390	1.40	105	111	3-Inch Chamber, FNA-UDMH.
1163	4-30-68	Impingement Pt.	Fan Plane	465	470	0.550	0.391	1.406	105	108	3-Inch Steel Chamber, FNA-UDMH.
1164	5-01-68	Impingement Pt.	Fan Plane	458	471	0.545	0.396	1.376	50	49	3-Inch Steel Chamber, FNA-UDMH.

---

*Note: Run numbers marked with an asterisk used a single unlike doublet injector with orifice diameters = 0.173 inch. The remaining run numbers used a single doublet with orifice diameters = 0.0986 inch.

Four pulsed laser reconstruction photographs have been made of each of the selected Phase I holograms (see Table I). The pictures were taken at reduced magnification of 3/8 in order to have the whole event on the same piece of film. The photographs of a given set differ from one another by a progressive bodily stepping of the copy camera in 1/2-inch increments away from the hologram. The first picture of the group corresponds to having the image of the 1/2-inch-wide iron bar (drilled with 1/4-inch holes on 1-inch centers) originally in the scene in focus. Quality of these photographs is excellent, and each differs from the other, as would be expected when photographs are taken at f/5.6. Examination of the negatives with a 125 X microscope showed that the granularity had a spacing of $\sim$30 microns. One can say that this is the minimum size particle which can be seen.

In addition, some photographs of holograms have been recorded at a magnification of 1:3/4. Most of these have been made of hologram B1115Q. Granularity of these photographs was of $\sim$24 micron size. Selected copies of some of these reconstruction photographs are shown in Figures 7 through 11. The maximum resolution was measured with a microscope to be 30 microns.

A similar method was followed in reconstructing and photographing holograms of combustion in the Phase II 3-inch-diameter acrylic thrust chambers (Table I). Approximately 7 reconstruction photographs were made of each of the 8 selected holograms. Representative of these reconstruction photographs are the illustrations in Figures 12 through 14 (Runs B1149, B1157 and B1162).

In evaluating the reconstructions, it was concluded that data reduction of four holograms would be attempted. The first was the water spray hologram from Run B1113W which is seen in Figure 7. In addition, two open flame tests, Runs B1115W (Figure 9) and B1117G (Figure 10) were selected to cover the two propellant combinations, namely FNA and UDMH and N_2O_4 and 50/50 N_2H_4-UDMH. Finally, a 3-inch-diameter acrylic combustion chamber run was also chosen (Run No. B1157, Figure 13).

As discussed subsequently, it proved virtually impossible to obtain drop size measurements from the 3-inch diameter acrylic combustion

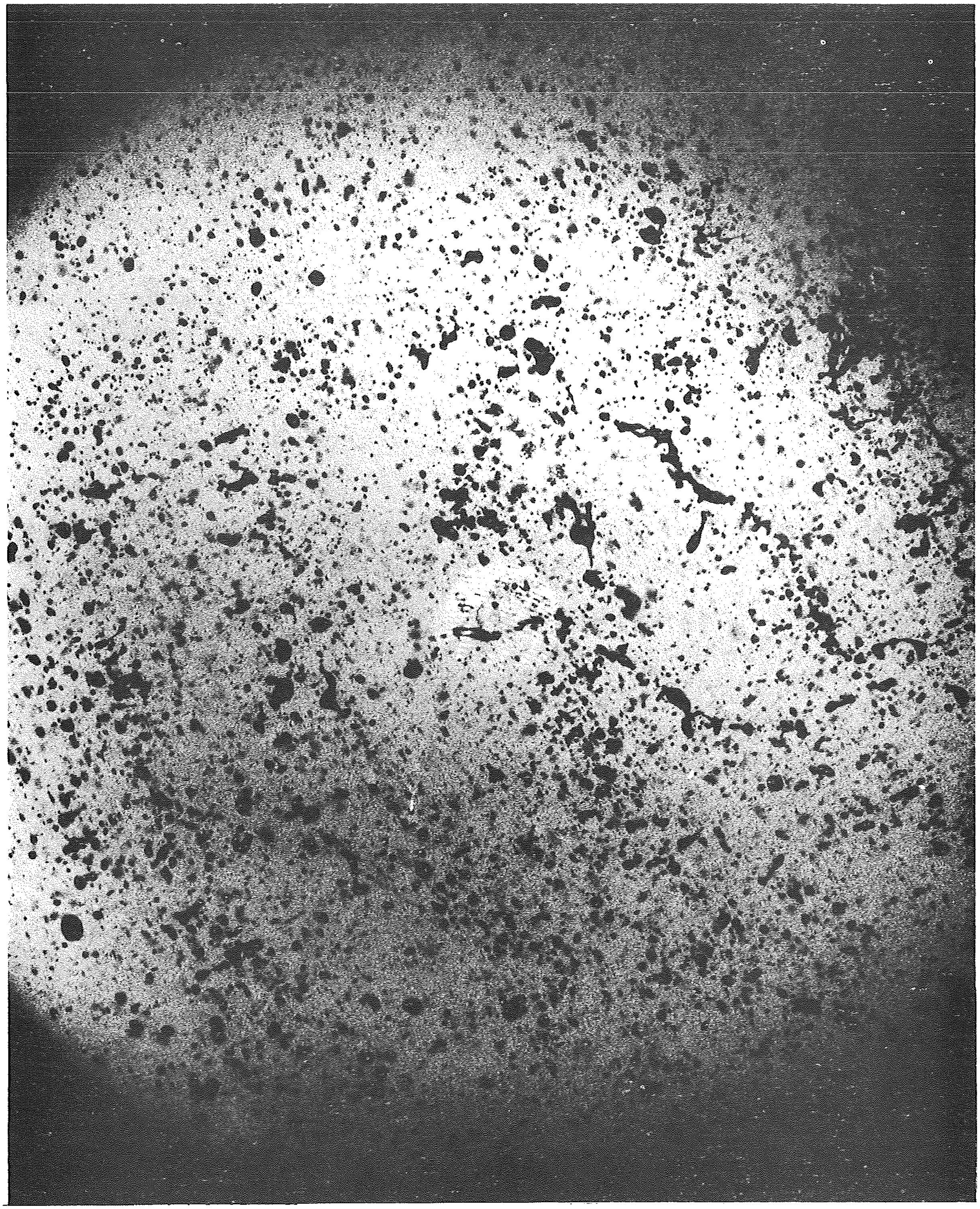

Figure 7 Copy of photograph of a pulsed ruby laser reconstruction of Hologram B1113W, originally made at JPL Edwards of a water spray pattern. The hologram was reconstructed with a ruby laser in the JPL holocamera. The photograph was recorded on SO243 film with the same camera used to make Figure 4. The size scale is the same as for Figure 8 on the following page.

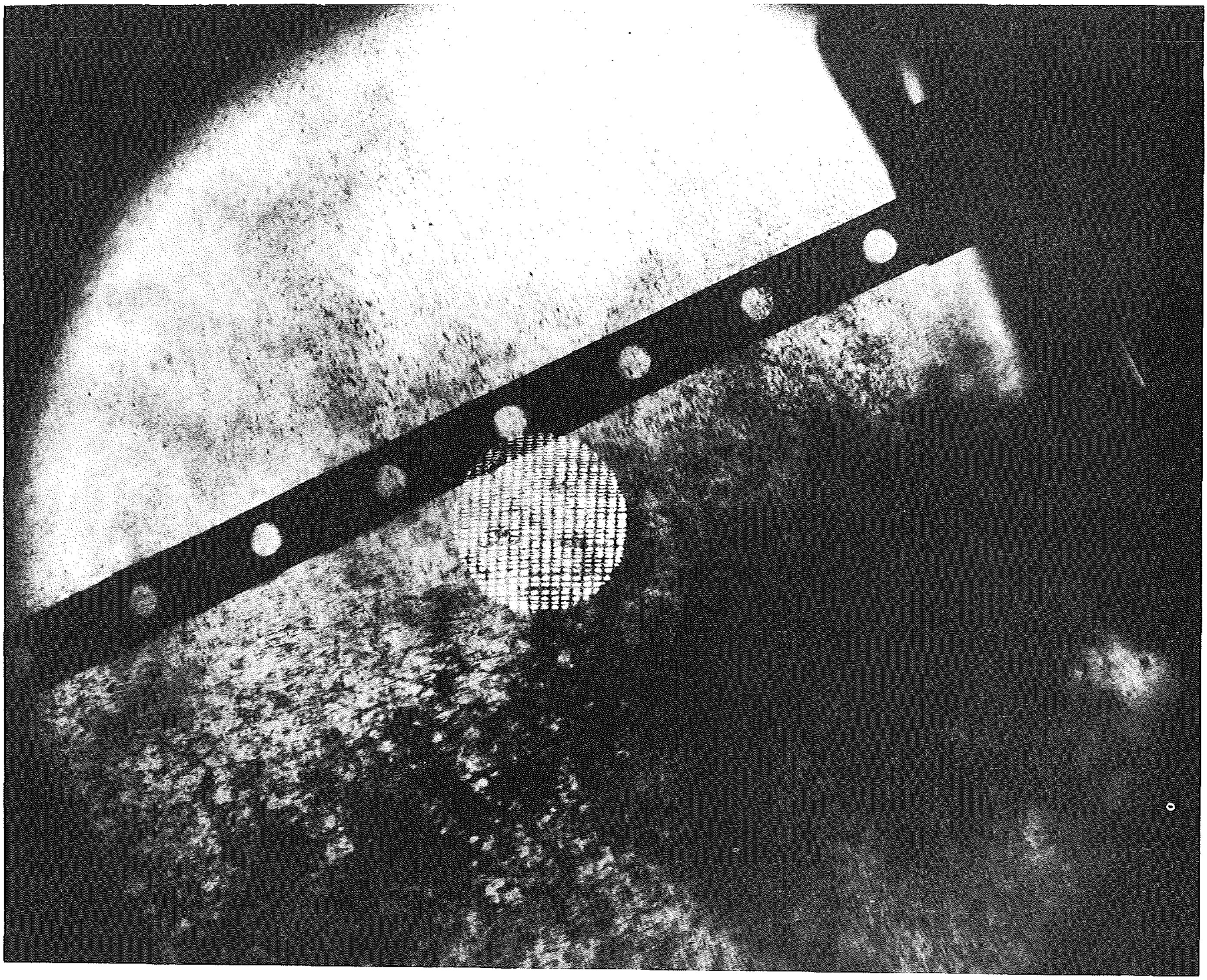

Figure 8. Copy of a photograph of a pulsed ruby laser reconstruction of Hologram B1115Q, originally made at JPL Edwards on 1-15-68 of the open flame combustion of N_2O_4 - 50/50 N_2H_4 UDMH propellant combination (1.2 and 1.5 lbs/second) flow rate, respectively, at 56/50 $^{\circ}$F. The photograph was recorded in the same manner and magnification as the one shown in Figure 7. The bar seen in the above picture was drilled with 1/4-inch holes on 1-inch centers.

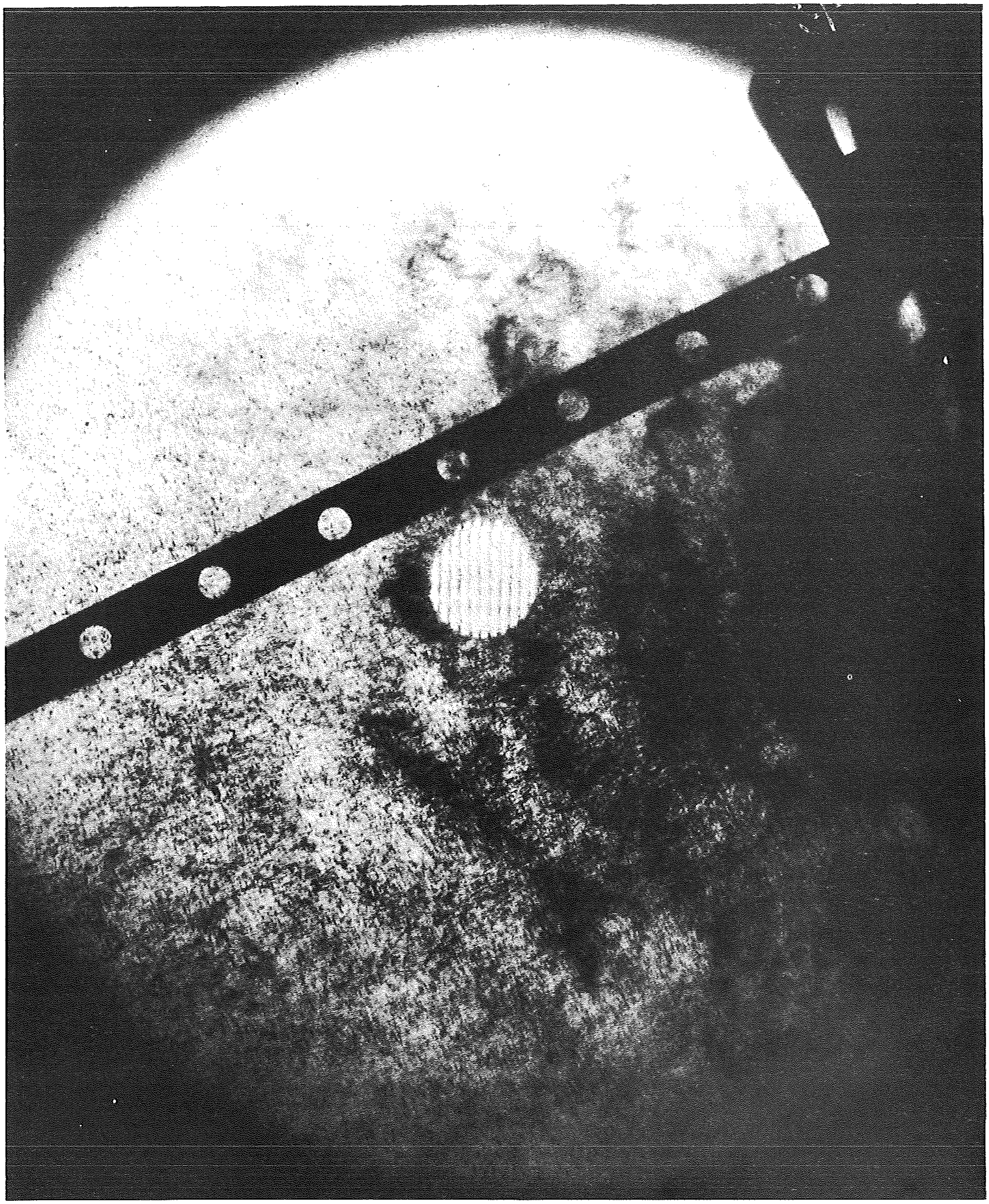

Figure 9. Copy of a photograph of a pulsed ruby laser reconstruction of Hologram B1115W, originally recorded on 1-17-68 at JPL Edwards of the open flame combustion of FNA and UDMH, flowing at 1.6 and 1.2 lbs/second. Photograph was recorded on SO243 Film.

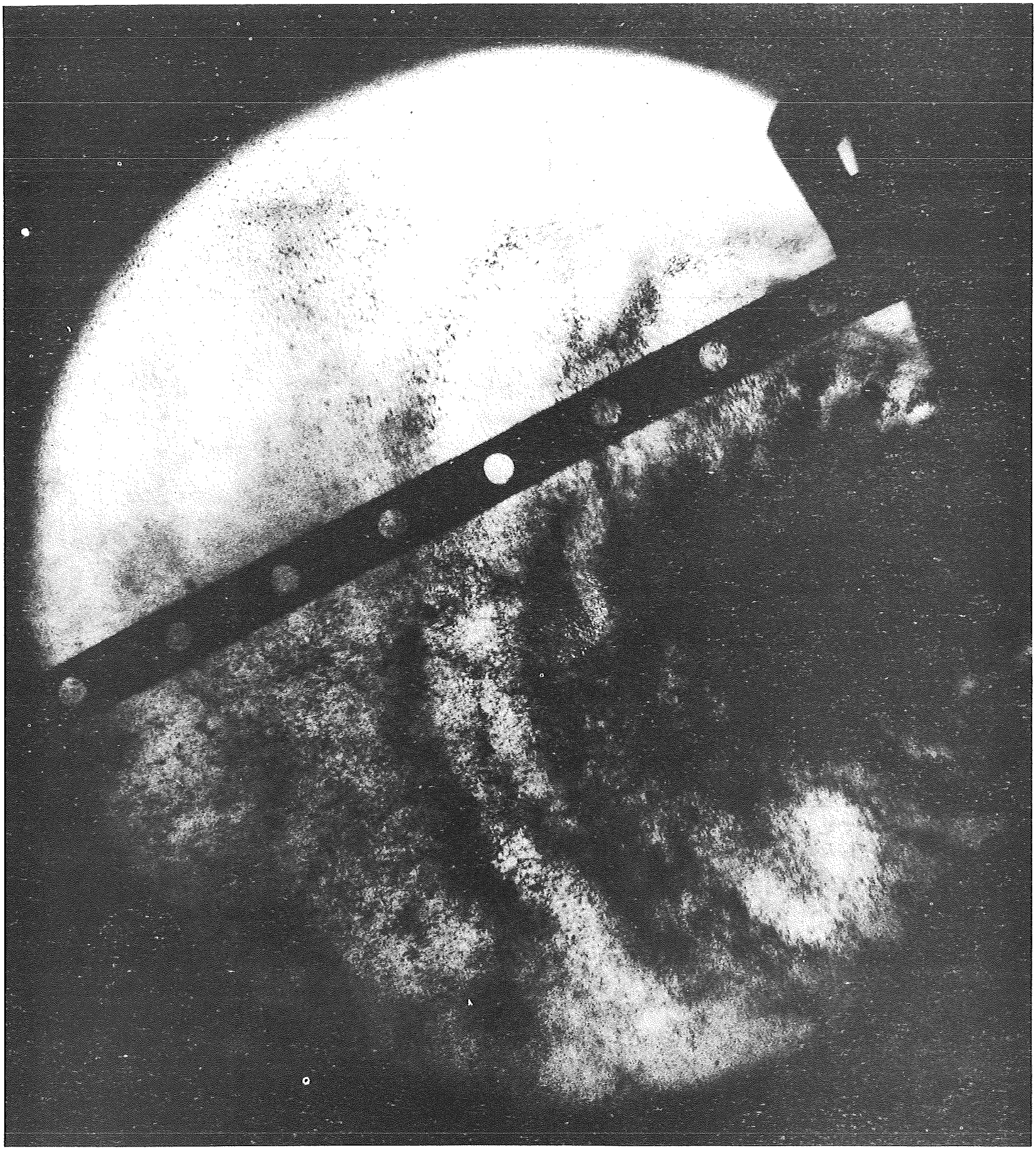

Figure 10. Copy of a photograph of a pulsed ruby laser reconstruction of Hologram B1117G, recorded originally on 2-6-68 at JPL Edwards of N_2O_4 - 50/50 N_2H_4 UDMH propellant combustion.

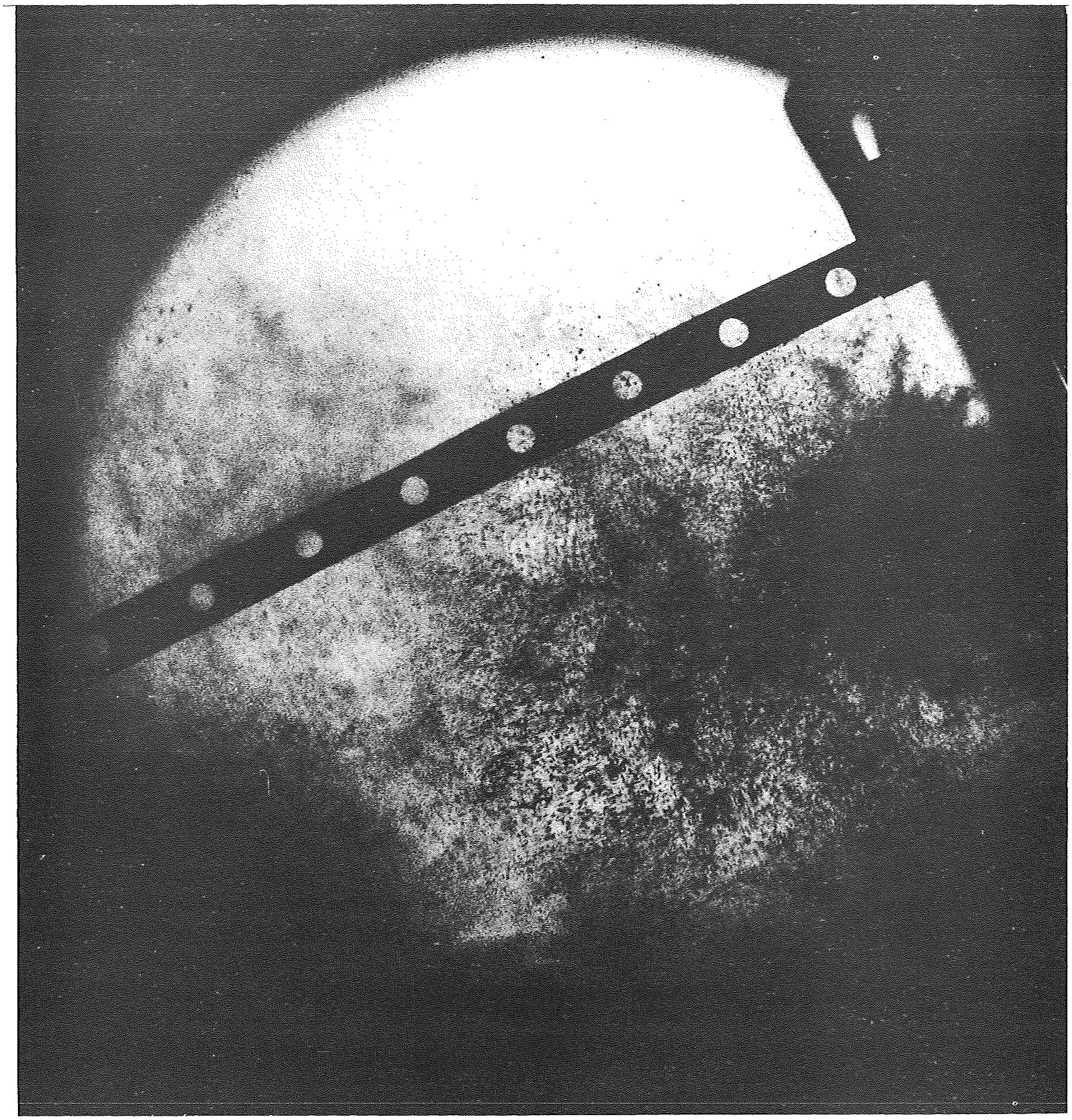

Figure 11. Copy of a photograph of a pulsed ruby laser reconstruction of Hologram B1115X, recorded originally on 1-17-68 of FNA-UDMH propellant combination, flowing originally at 2.0 and 0.9 lbs/second (53/56°F).

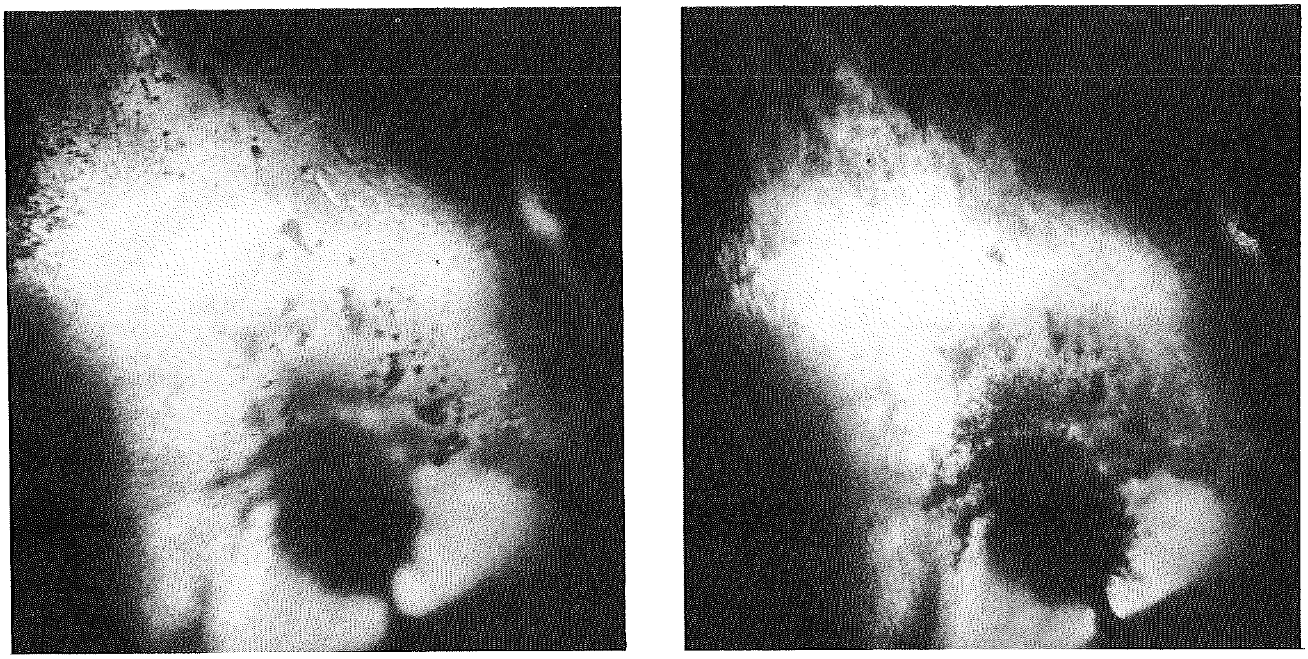

Figure 12. Two photographs of the reconstruction of a hologram of hypergolic propellant combustion in a 3-inch inside diameter combustion chamber with 0.099-inch injector orifices. The photographs correspond to different focal settings of the copy camera. The photographs are of Run B1149 using N_2O_4 and 50/50 N_2H_4-UDMH propellants.

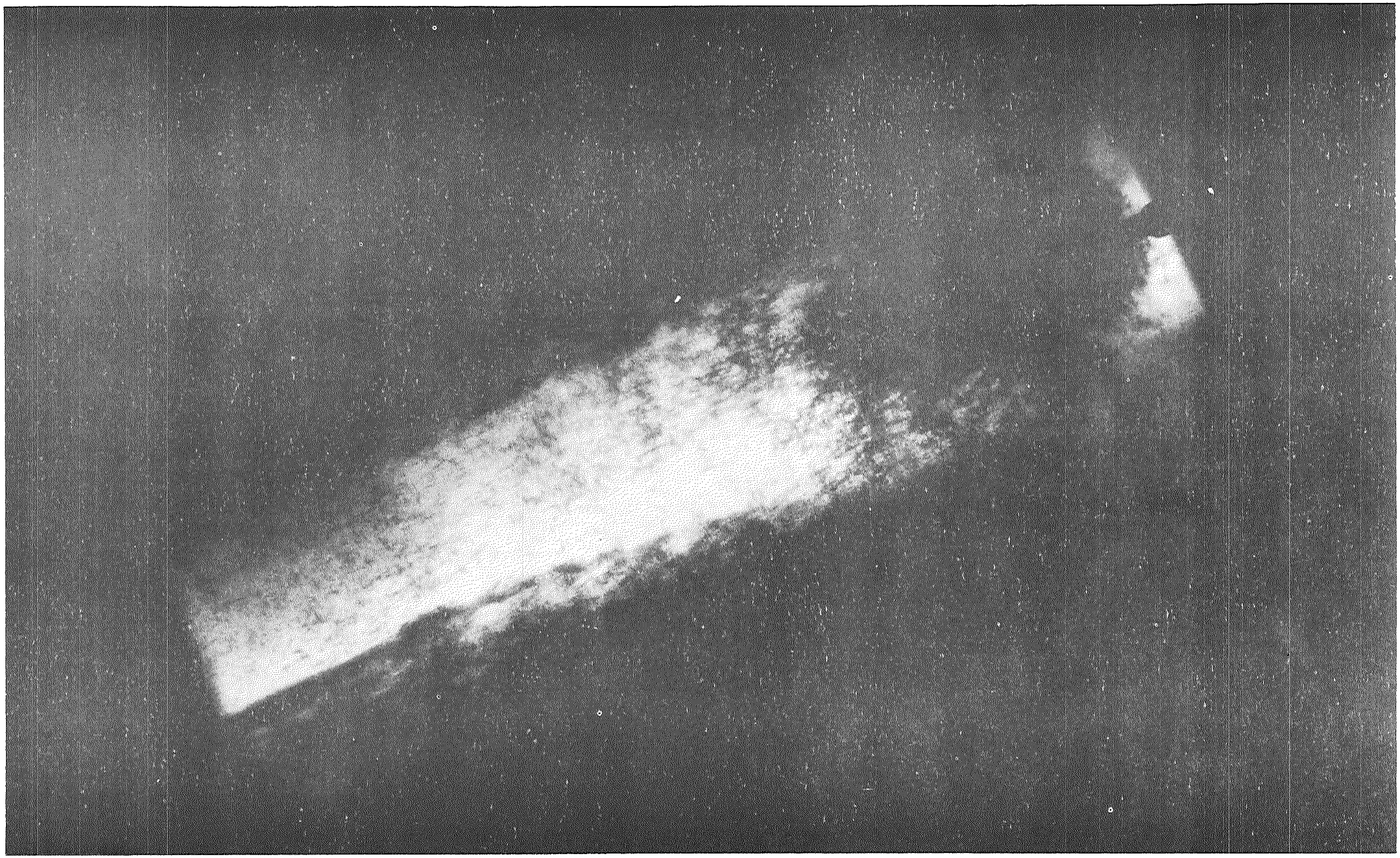

Figure 13. Reconstruction photograph from ruby laser hologram of test B1157. The photo shows the fan plane from an FNA/UDMH combusting spray in a 3-inch diameter acrylic combustion chamber.

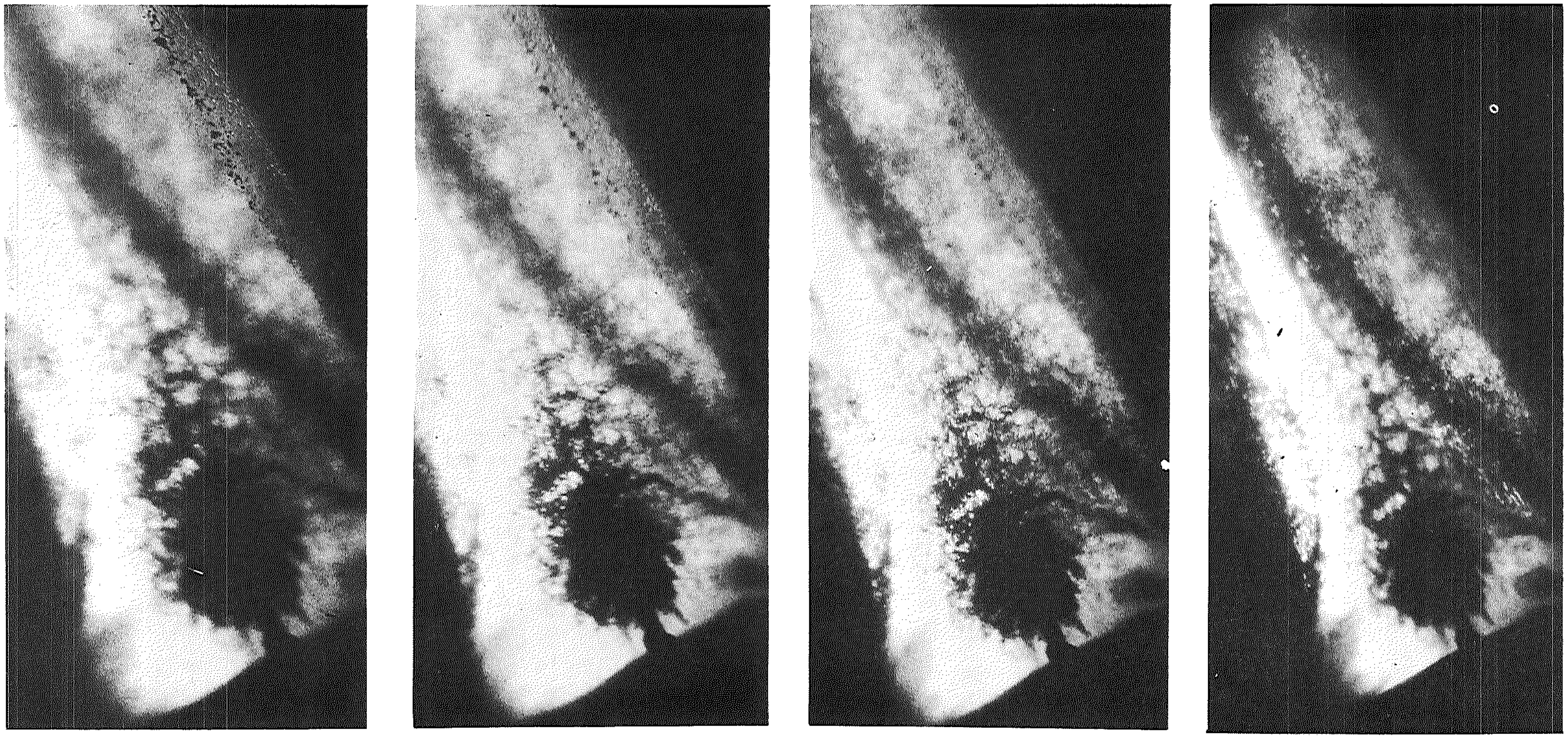

Figure 14. Four photographs of the reconstruction of a hologram of combustion within a rocket engine. The four photographs correspond to different focusing of the camera throughout the reconstruction volume. For the left picture, the camera was focused on the near inner wall. For the right picture, the camera was focused on the far inner wall. The other photos were at intermediate locations in the region of the fan. The hologram was No. B1162 and was the best of the Phase II series. The propellant was FNA and UDMH.

chamber hologram reconstruction (Run B1157, Figure 13). As an alternate, a reconstruction photograph of combustion in a windowed thrust chamber from another program was selected for data reduction.* A reconstruction photograph of combustion in the windowed chamber made during the Air Force program is shown in Figure 15. The illustration is of N_2O_4 and 50/50 N_2H_4-UDMH burning at a pressure of 166 psia, mixture ratio of 2.6 (O/F) and total propellant mass flow rate of 0.39 lb/sec.

2.4 DATA REDUCTION TECHNIQUE

Droplet size measurements were made using a Gaertner Scientific Company measuring microscope (Model 12-35A). The micrometer slides of the microscope can be read to within 0.0001 inch. The overall magnification used for most of the measurements was 15 X. A higher magnification (30 X) was found to be less satisfactory for the open flame and combustion chamber tests, in that the contrast between the droplet and the background diminished. All photographs of the reconstructed holograms were analyzed using the 15 X magnification except for water flow test B1113W, Position 1 (observer #2) and Position 2, for which 30 X magnification was used.

Both negatives (Eastman Type SO-243) and positive prints made from the negatives were studied under the microscope. Positive prints such as Figure 16 have the advantage of allowing measurement of dark droplet outlines on a white background, which is more natural for most people, compared to the white droplets on a dark background (Figure 17) with the negatives. However, droplet resolution is reduced with the positives. Nearly all measurements were made using negatives (Table II) illuminated from the back. This improved contrast of the white droplets on the speckled, dark background compared to front lighting. The equivalent diameter of the background granularity (the white areas in the background on the negatives) is within the range of approximately 20 to 70

---

*Air Force Contract F04611-69-C-0015: "Laser Holocamera Droplet Measuring Device," Final Report AFRPL-TR-69-204, November 1969.

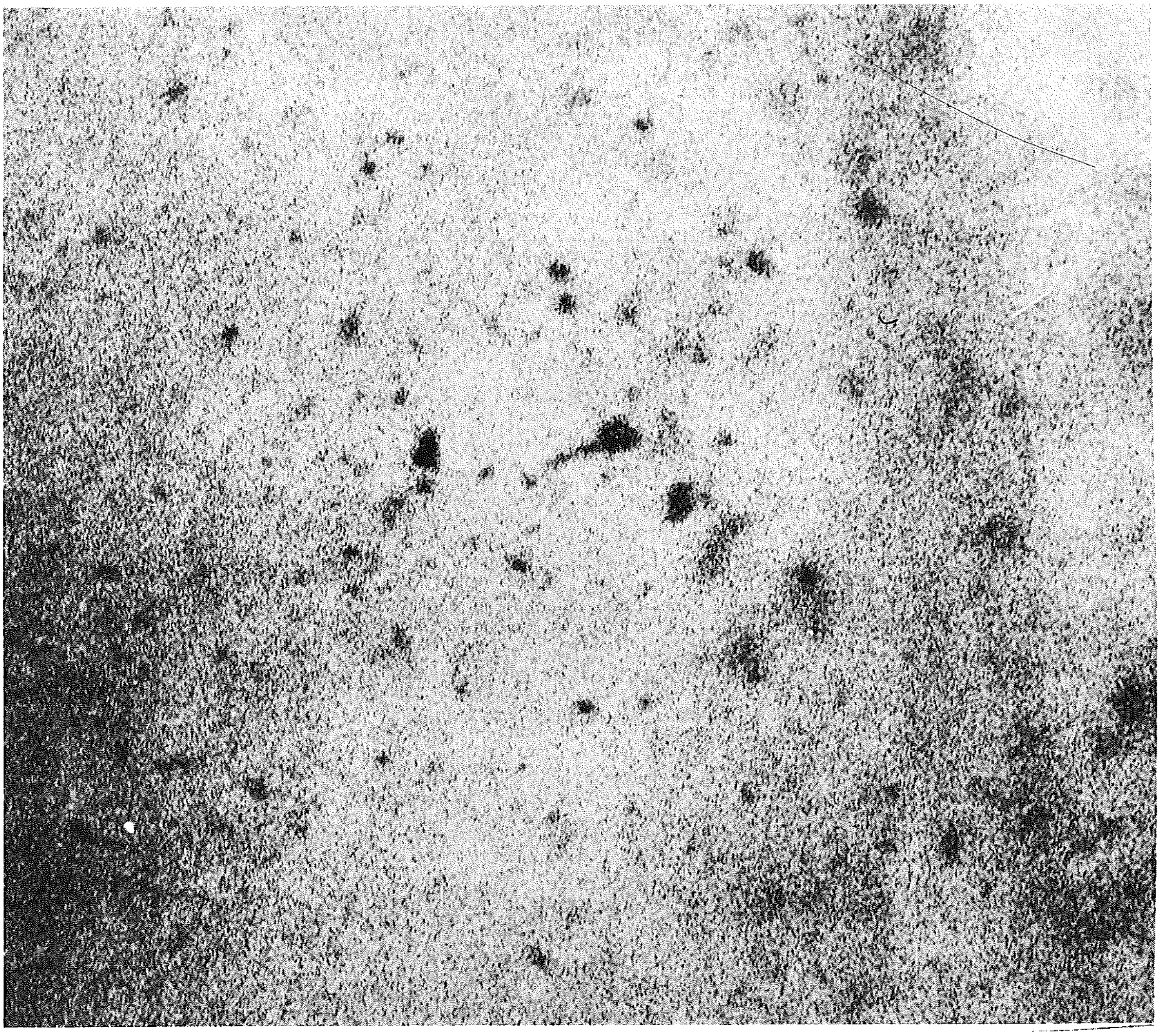

Figure 15. Droplet dispersion (Test A4-100) photographed from a ruby laser reconstruction of a ruby laser hologram. The original scene was a reacting spray of N_2O_4 and 50/50 N_2H_4-UDMH propellants in a windowed thrust chamber operating at a chamber pressure of 166 psia and mixture ratio of 2.68. Magnification of this photograph is approximately 12X. Direction of flow is from left to right. (Illustration courtesy of the Air Force Rocket Propulsion Laboratory, Contract F04611-69-C-0015).

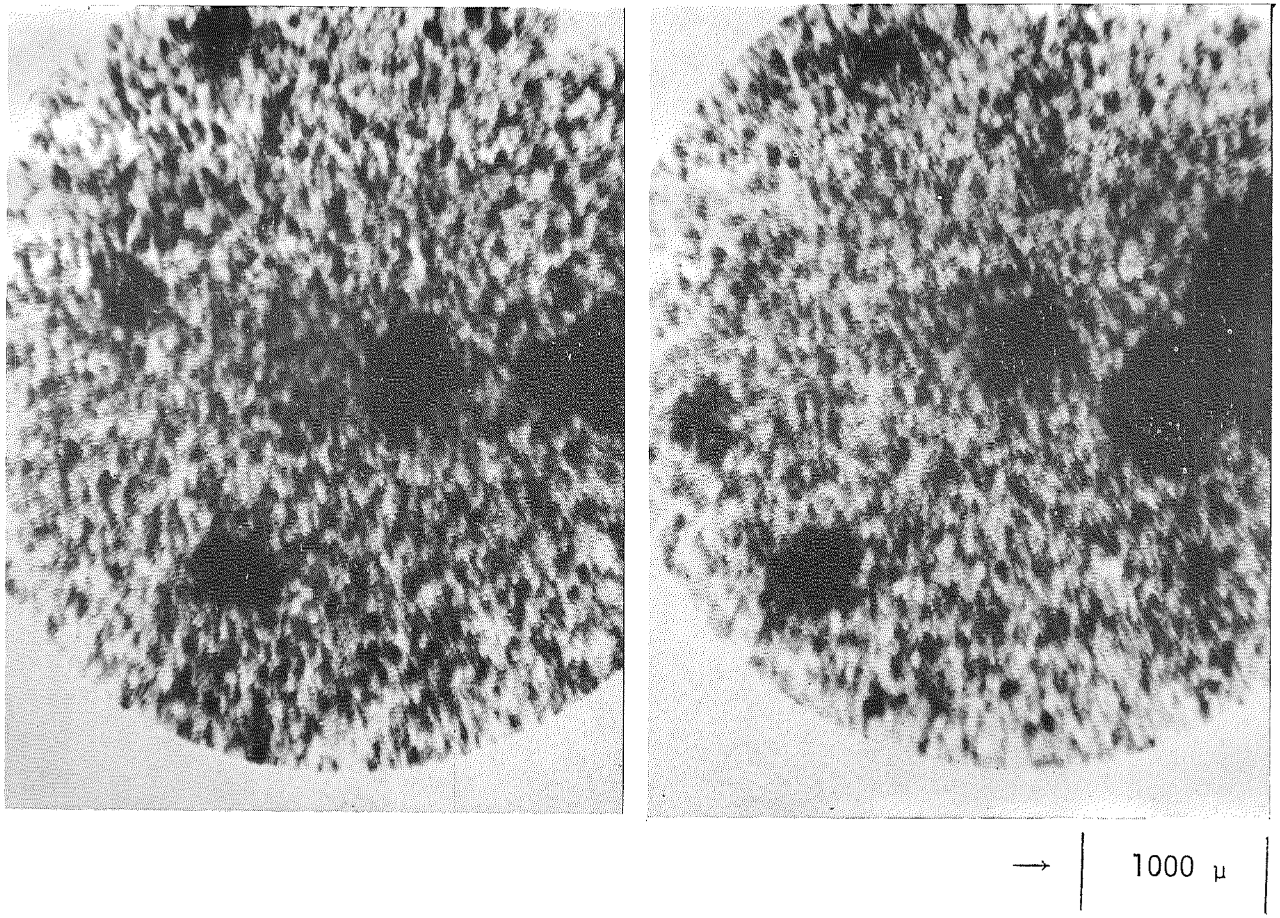

Figure 16. Positive photomicrographs of portions of an SO243 photograph of a pulsed ruby laser reconstruction of Hologram B1113W, originally made at JPL-Edwards of a water spray fan.

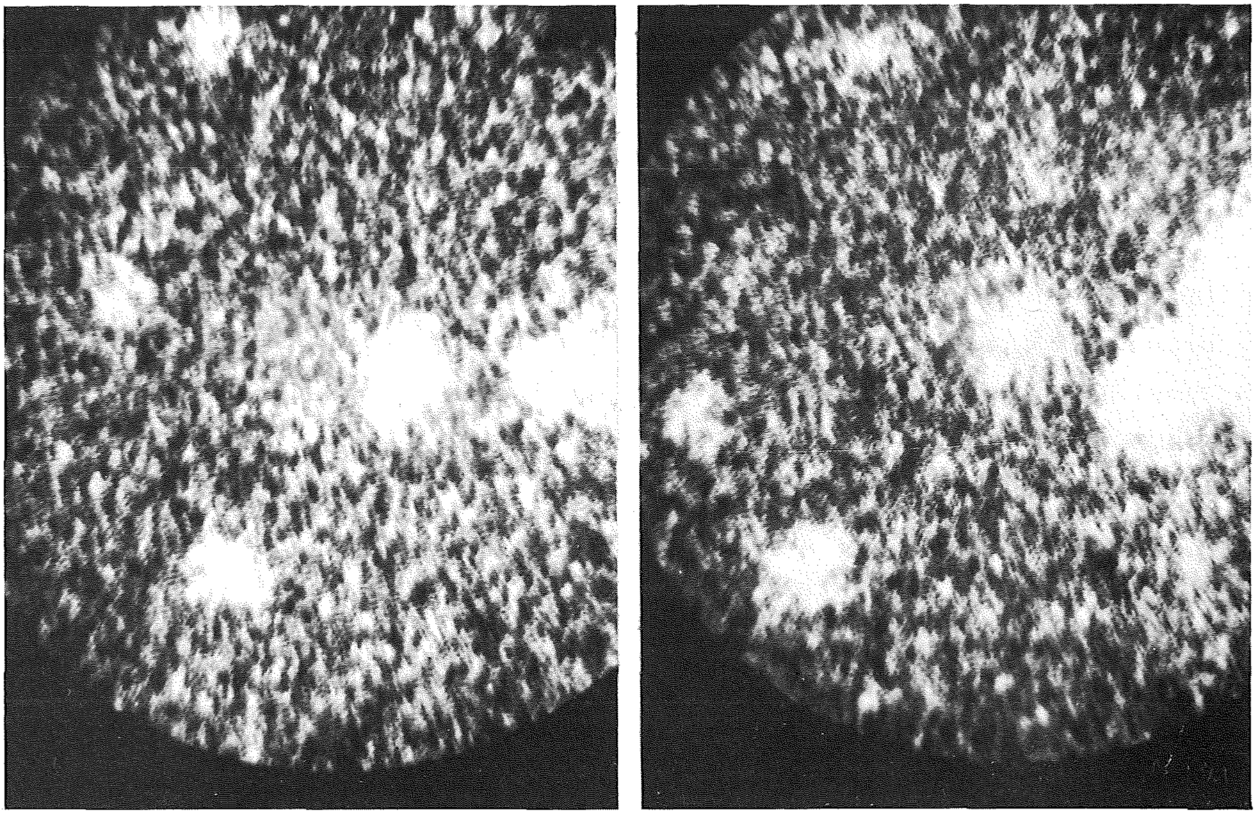

Figure 17. Negative photomicrographs of portions of an SO243 photograph of a pulsed ruby laser reconstruction of Hologram B1113W of a water spray fan. This is the same subject matter as the preceding figure and shows the difference between viewing positive prints and negatives.

microns, with a Sauter mean diameter, D_{32}, of 55 microns. Background granularity was determined by measurements with a positive print made from the reconstructed hologram for combustion chamber Test B1157 (See Table II on page 30).

Data reductions were made in all cases with photographs of holograph reconstructions of planes looking at the doublet fan. Although it was desirable to make droplet counts about the center region of the fan downstream of ligament breakup, examination of the negatives indicated that very few distinct droplets could be seen in the center region for the open flame tests just downstream of ligament breakup. The droplet count locations selected represent regions where an appreciable number of droplets could be seen. This required that droplets be measured in regions considerably removed from the fan centerline for the open flame tests (for example, see Figures 8 through 11). All droplets which could be seen in the areas selected for data reduction were measured and recorded. Most droplets appear non-circular without sharply defined boundaries. An equivalent diameter of each droplet was estimated using the microscope by visualization of an equivalent circular area equal to the droplet area. Approximately 40 hours of time were spent in actual measurement of droplet diameters. It was found that once data reduction areas were selected, careful total droplet measurements could be completed within a few hours of elapsed time.

The raw data, in terms of all droplet diameters in inches, was input to a computer program which multiplied the data by a scale factor which accounted for the magnification of the photographs analyzed, counted the droplets in intervals of 25 microns; i. e., 50-74.99, 75 to 99.99, etc., and computed the cumulative volume fraction, normalized diameter, D_{30}, and D_{32} based upon the midpoint diameter in each 25 micron interval. Droplets above approximately 2000 microns in diameter were arbitrarily excluded in the data reduction except for the water spray distribution. At 12 inches downstream of the injection plane, where droplet measurements were made for the water flow test, droplets (or ligaments) larger than 2000 microns were dispersed non-uniformly through a plane in the spray field. Droplet measurements were made with photographs which were 2.60 times smaller than actual size for the water flow and open flame tests and 1.5 times larger than actual for the combustion chamber test.

The experimental data are presented in terms of D_{30} and D_{32} computed from the data, cumulative volume fraction, $\Sigma\, nD^3 / (\Sigma\, nD^3)$ total, versus a normalized droplet diameter, D/D_{32}, and the number of droplets counted in each 25 micron diameter increment versus droplet diameter. Curves drawn through the data are based on a commonly used unimodal droplet size distribution fitted to the experimental data. These are discussed in Section 3.2. The normalization is based on the Sauter mean diameter:

$$D_{32} = \Sigma\, n_i D_i^3 / \Sigma\, n_i D_i^2 \qquad (2)$$

This diameter is considered most significant for combustion models since droplet volume is proportional to the energy release time in combustion and droplet evaporation is a function of droplet surface area. The measured mean droplet diameters are compared with available mean droplet diameter correlations which are based on orifice diameters, jet velocities, impingment angle, and liquid physical properties in Section 3.1. Precision of the data and confidence levels for these relatively small droplet counts are discussed in Section 3.4.

2.5 EXPERIMENTAL RESULTS

Droplet size distributions and mean diameters computed from the test data are presented for one water flow test (B1113W), two open flame tests (B1115W, with FNA/UDMH propellants and B1117G, with N_2O_4/0-5 N_2H_4-0.5 UDMH propellants) and one combustion chamber test (A4-100, with N_2O_4/0.5 N_2H_4-0.5 UDMH propellants)*. The total droplet counts and the experimental values of the volumetric mean diameter, D_{30}, and the Sauter mean diameter, D_{32}, are listed in Table II. The water flow and open flame test apparatus and conditions for the droplet measurement analysis are given in Figure 18. Conditions for the combustion chamber tests are presented in Figure 19. The droplet measurement region

---

*The combustion chamber Hologram No. A4-100 was furnished courtesy of Air Force Contract F04611-69-C-0015, Air Force Rocket Propulsion Laboratory, Edwards Air Force Base.

Table II. Comparison of Measured Mean Droplet Sizes with Predicted Values Based on Existing Empirical Correlations

Test	Position	Propellants	Photo Type	Total Count	Droplet Size, Microns						
					Measured			Predicted			
					D30	D32	$\bar{D}$	$\bar{D}^{(a)}$	D30$^{(b)}$	D30$^{(b)}$	D30$^{(c)}$
									$\Delta V = 0$ 90°	$\Delta V = V_j$ 90°	$\Delta V = V_j$ 45°
<u>Cold Flow</u>											
1113 W	2	H_2O	Positive	495	891	1138	1380	564	915	343	700
1113 W	1	H_2O	Negative	179	726	942	1040	564	915	343	700
1113 W	1	H_2O	Negative	146	692	893	998	564	915	343	700
<u>Open Flame</u>											
1115 W	1	FNA/UDMH	Negative	218	413	465	493	176 (fuel)	386	138	282
1115 W	2	FNA/UDMH	Negative	47	450	503	514	176 (fuel)	386	138	282
1117 G		$N_2O_4/.5N_2H_4$ - .5 UDMH	Negative	240	725	839	938	259 (fuel)	575	204	416
<u>Combustion Chamber</u>											
B 1157		FNA/UDMH	Positive	105	50	55		167	310	134	264
						(Background Granularity Size)					
A 4100		$N_2O_4/.5N_2H_4$ - .5 UDMH	Negative	64	258	315	353	516 (fuel)	611	344	495 (62°)

(a) Mass median based on Rocketdyne correlation for 60 degree impingement corrected for physical properties but not for smaller impingement angle (45 degrees) for Runs B 1113 W, B 1115 W, and B 1117 G.

(b) Based on Ingebo correlation, corrected for liquid physical properties for fuel side but not for impingement angle.

(c) Corrected for impingement angle and physical properties.

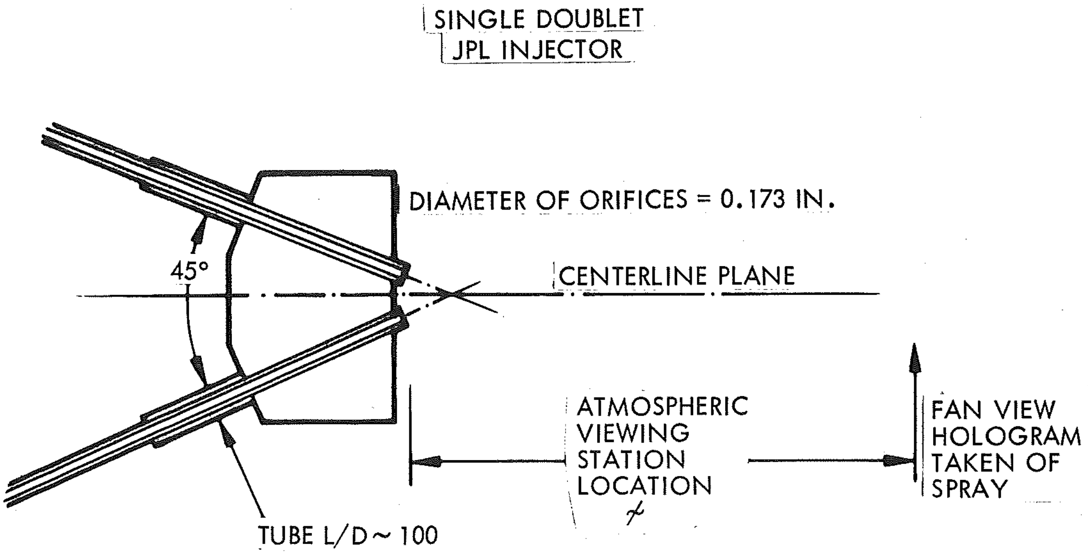

RUN NO.	TEST DATE	PROPELLANTS	TOTAL FLOW (LB/SEC)	O/F	INJECTION VELOCITY (FT/SEC)		PROP. TEMP. (°F)		ℓ (IN.)	SCENE* DIA. (IN.)
					F	OX	F	OX		
B1113W	12-6-67	WATER	2.390	1.000	118	118	-	-	12	10
B1115W	1-17-68	FNA/UDMH	2.768	1.380	142	98	52	53	4	9
B1117G	2-6-68	N_2O_4/.5 N_2H_4-.5 UDMH	2.813	1.254	140	108	98	95	4	9

*HOLOGRAM RECONSTRUCTED IN CENTERLINE PLANE.

Figure 18. Water flow and open flame test apparatus and conditions for hologram analysis.

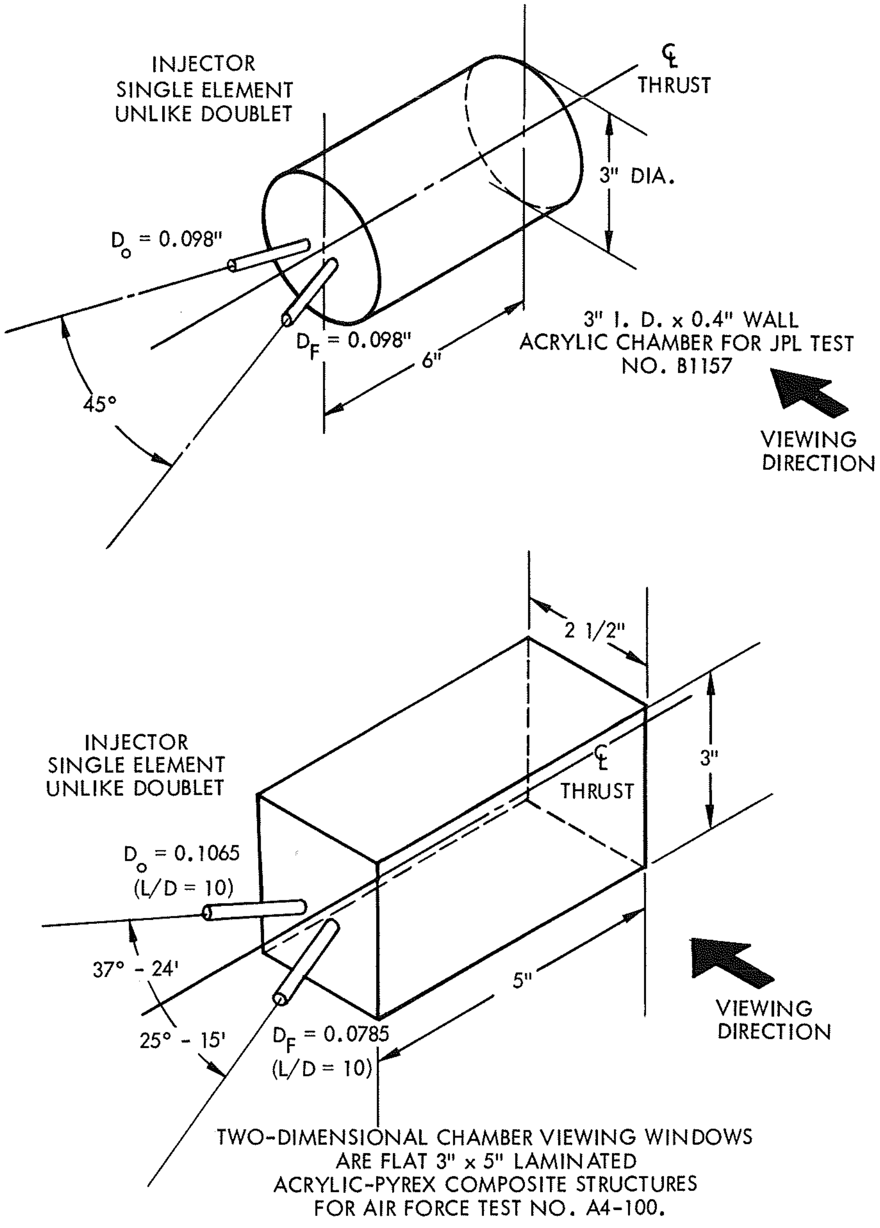

RUN NO.	TEST DATE	PROPELLANTS	TOTAL FLOW (LB/SEC)	$\frac{W_o}{W_F}$	Pc (PSIA)	C* (FT/SEC)	V_F (FT/SEC)	V_{OX} (FT/SEC)	T_F (°F)	T_{OX} (°F)
B1157	4-29 68	FNA/UDMH	0.847	1.566	104	3500	126	99	40	35
A4-100		N_2O_4/.5N_2H_4 -.5UDMH	0.39	2.68	166	2500	56	51	60	60

Figure 19. Combustion chamber test apparatus and conditions for hologram analysis

locations are presented in Figure 20.

Cumulative volume fraction versus D/D_{32} and droplet number-diameter data are presented in Figure 21 through 32. The curve fits for both types of data presentation are discussed in Section 3.2. Droplets for B1113W in Position 1, a square region 0.5 inch by 0.5 inch on the 4-by 5-inch negative which corresponds to a 1.7-in^2 area in the spray field, were measured by two different observers. These data are shown on the same cumulative volume fraction and number diameter figures for comparison (Figure 21 and 22). The two sets of data compare closely in terms of the cumulative volume fraction which, because it is an integration process, tends to smooth the data. Variation in data between the two observers is more evident in the number-diameter comparison which is a function of the derivative of the cumulative distribution form. The difference between D_{30} or D_{32} for the two sets of data is approximately 5 percent. Although all drops in Position 1 were measured, the two observers differed by approximately 20 percent in total droplet count. This is attributed to one observer measuring some fainter appearing, or less well-defined, drops somewhat out of the plane of focus of the particular holographic reconstruction.

All drops were measured in a larger area surrounding Position 1 for Test B1113W, (Figures 23 and 24). The number-diameter characteristic for this larger population of 495 appears better defined than the Position 1 population. The Position 2 population contains a higher percent of large equivalent diameter drops than the Position 1 population, which results in a larger mean diameter by approximately 200 microns for Position 2. These few large droplets, which are plainly visible in Figure 7, have a pronounced effect on D_{30} and D_{32}. All droplets exceeding 2000 microns were arbitrarily excluded from the water flow measurement data, even though at 12 inches downstream from jet impingement approximately 12 droplets exceeded 2000 microns in the 495 droplet population. The large droplets result from cold flow tests with water, which has high surface tension and from the low 45-degree impingement angle.

The cumulative distributions for droplet measurements for the open flame tests (Figures 25 through 30) are very similar to those for the water

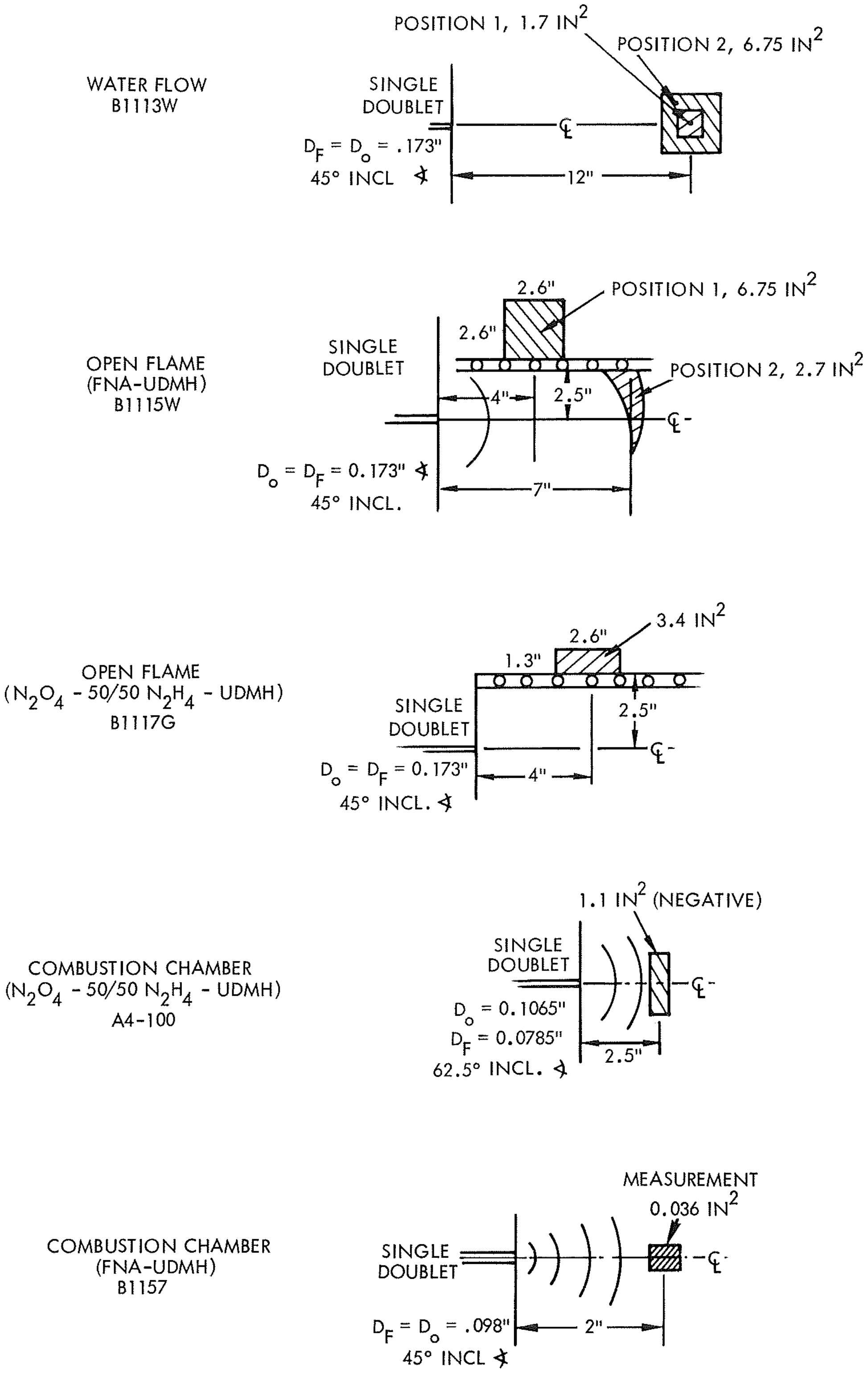

Figure 20. Droplet count locations and areas on hologram reconstruction photographs for each test run number

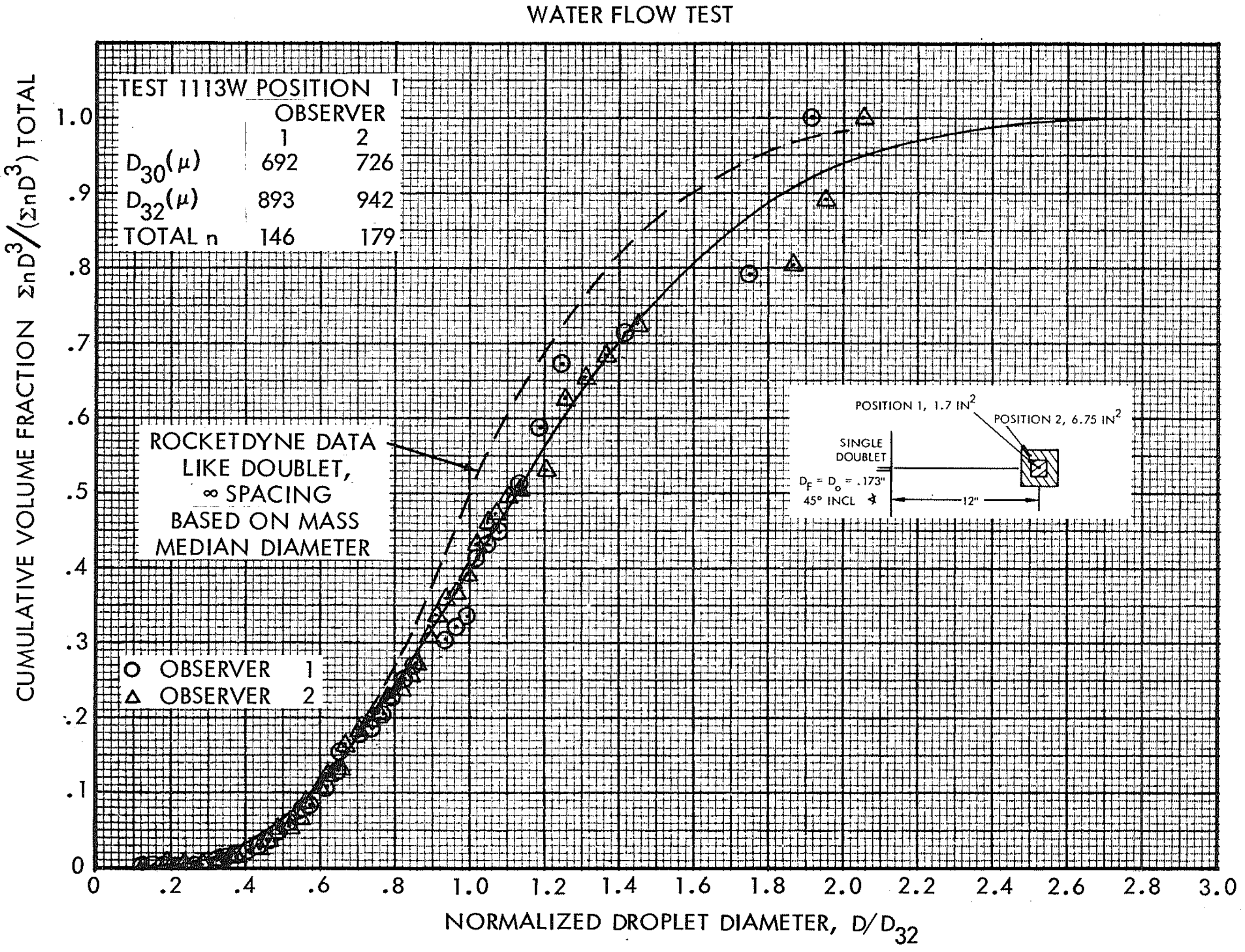

Figure 21. Experimental cumulative volume fraction versus normalized droplet diameter for water flow test B1113W, position 1. The curve drawn through the data is based on fitting the General Exponential size distribution to the cumulative volume fraction.

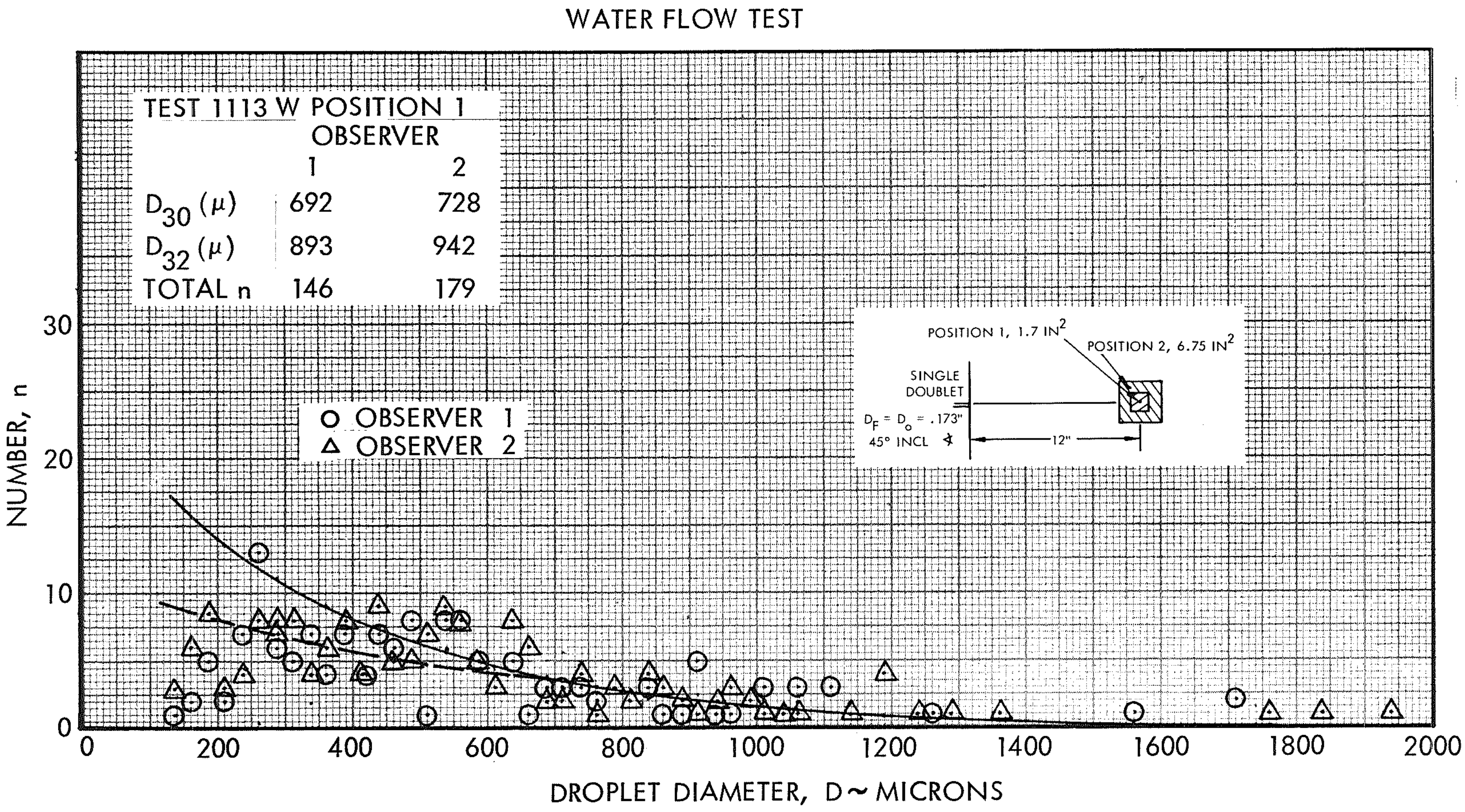

Figure 22. Experimental droplet count in 25 micron interval versus droplet diameter for water flow test B1113W, position 1. The solid line curve is based on a derivative of the curve fit of the cumulative data. The dashed line is based on a closer fit of the lower end of the cumulative distribution.

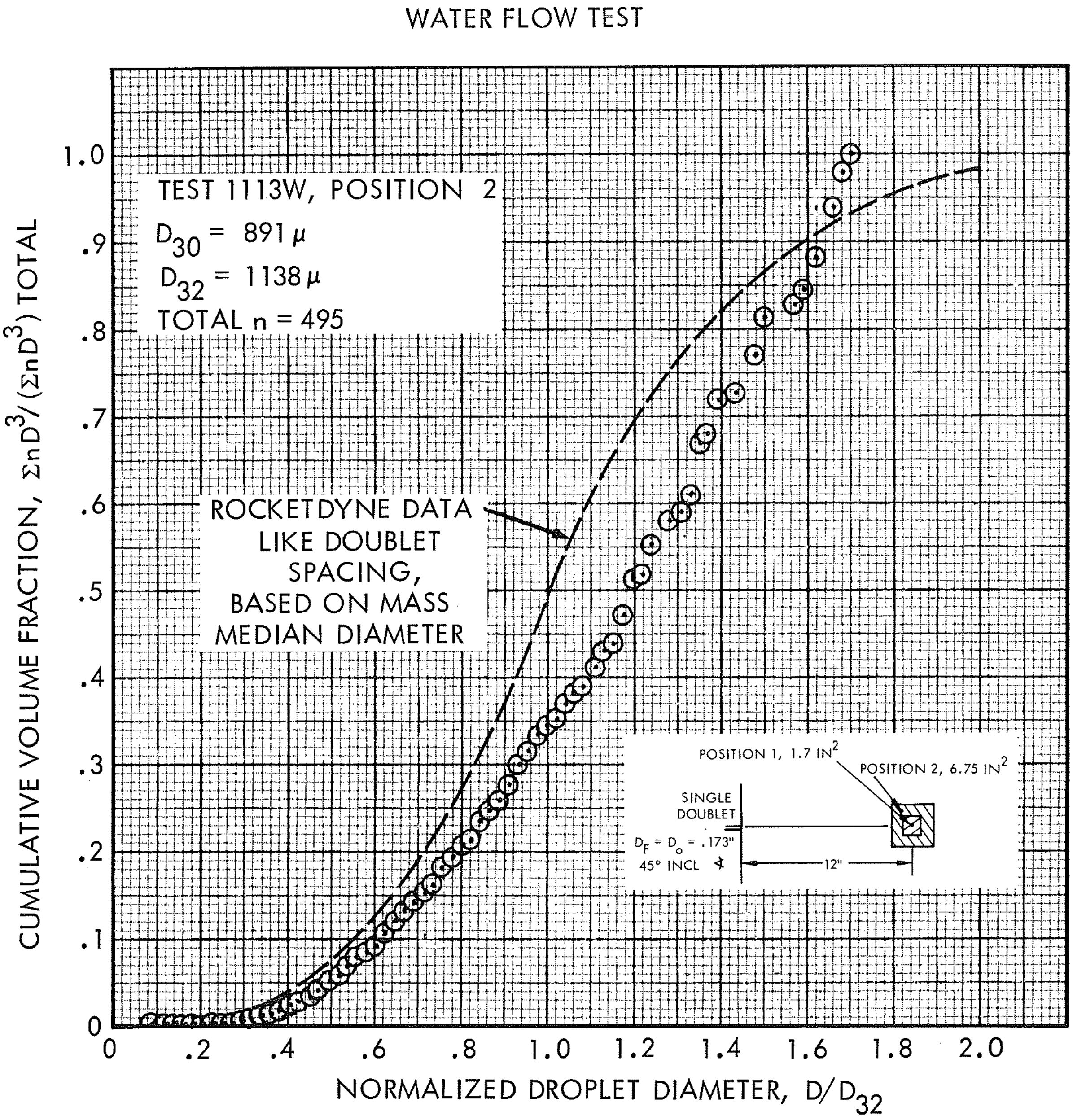

Figure 23. Experimental cumulative volume fraction versus normalized droplet diameter for the water flow test B1113W, position 2.

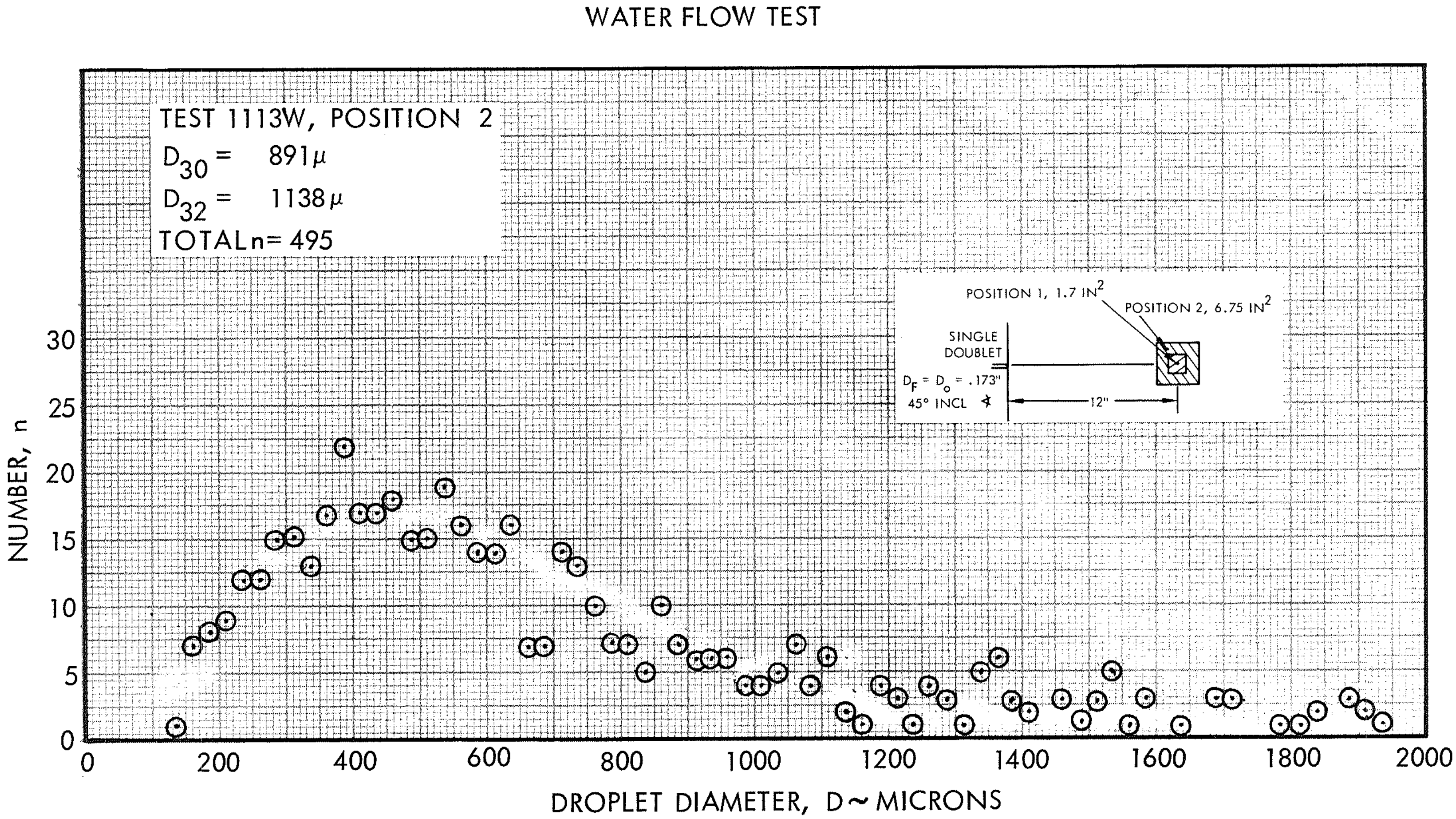

Figure 24. Experimental droplet count in 25 micron interval versus droplet diameter for water flow test B1113W, position 2.

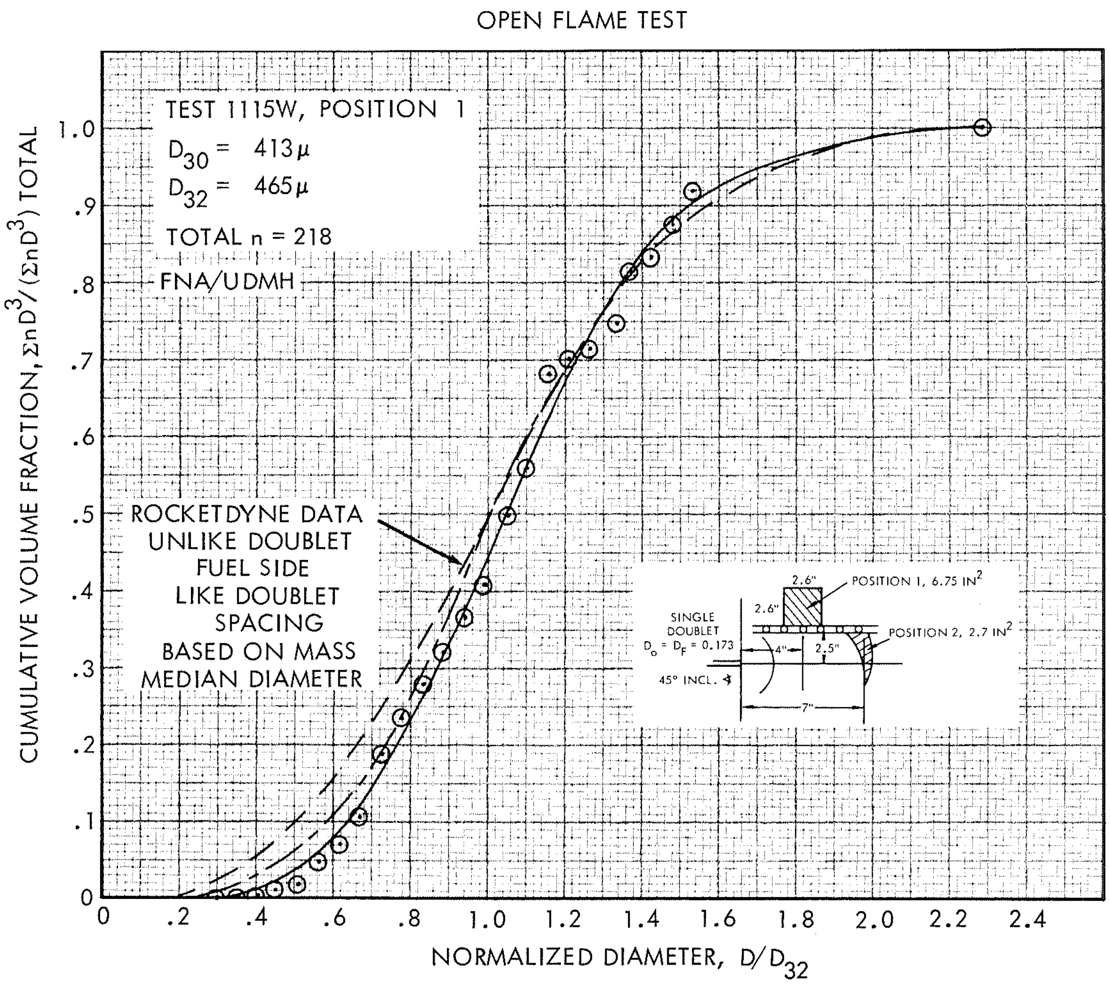

Figure 25. Experimental cumulative volume fraction versus normalized droplet diameter for open flame test B1115W, position 1, with FNA/UDMH propellants.

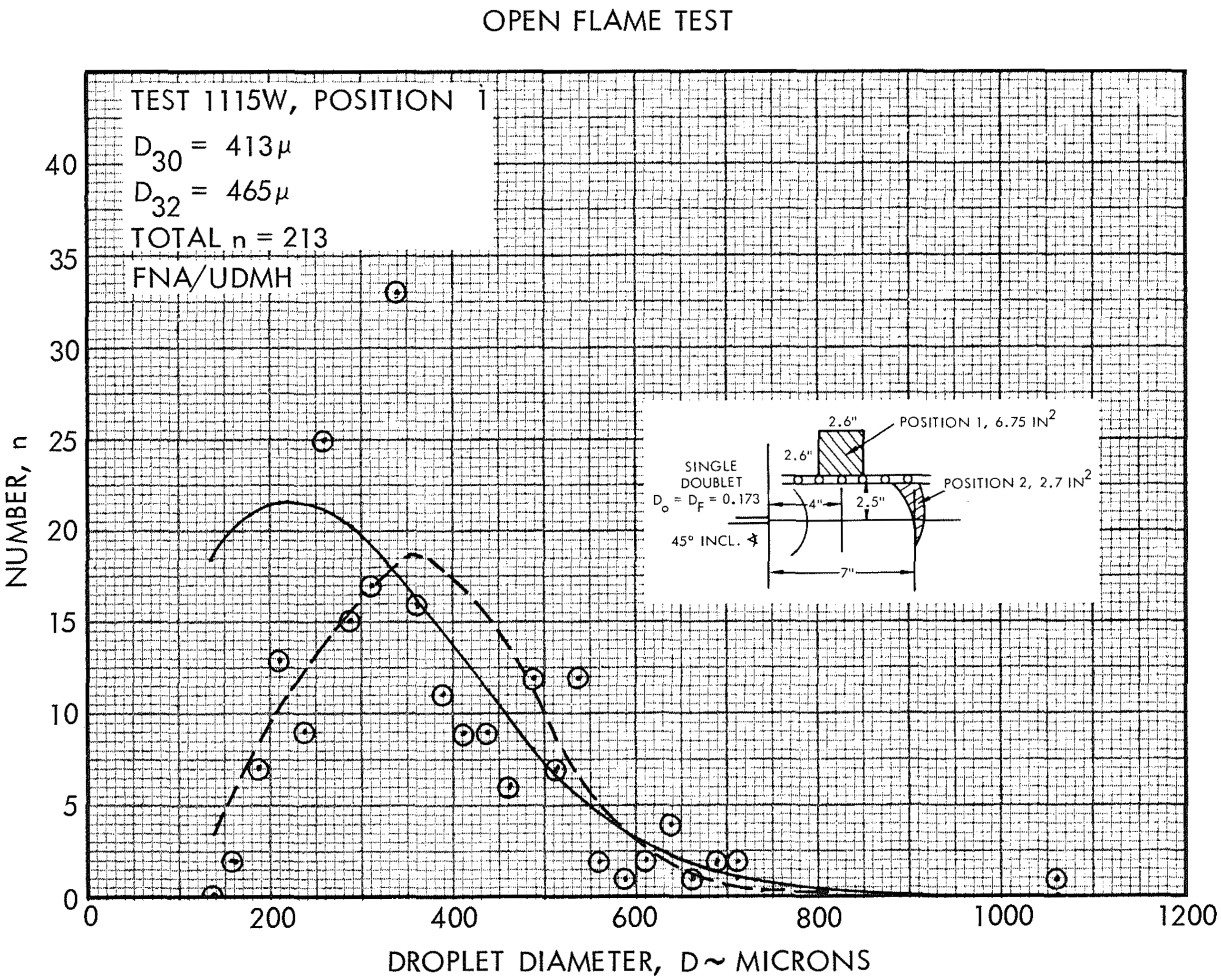

Figure 26. Experimental droplet count in 25 micron interval versus droplet diameter for open flame test B1115W, position 1, with FNA/UDMH propellants.

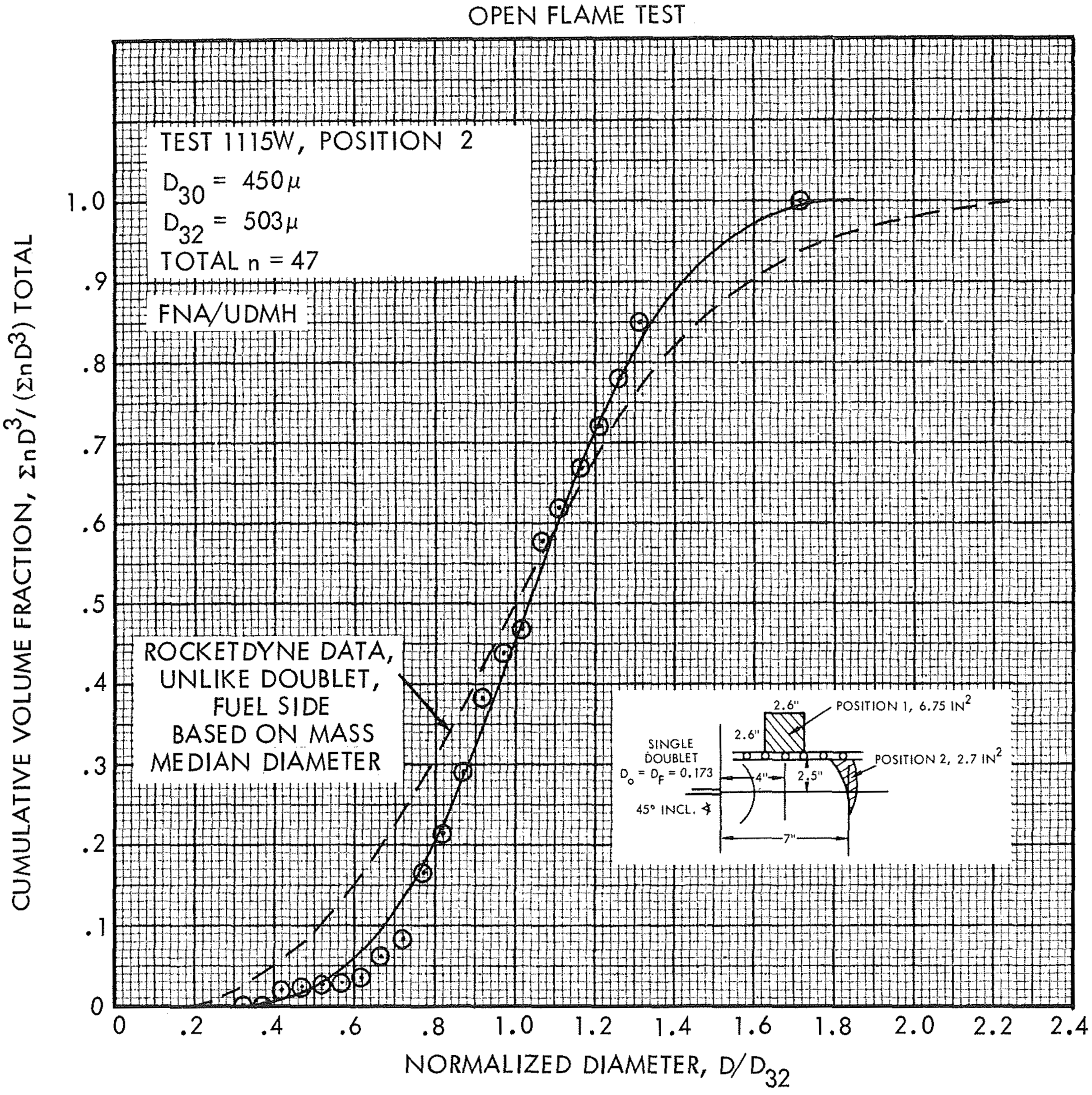

Figure 27. Experimental cumulative volume fraction versus normalized droplet diameter for open flame test B1115W, position 2, with FNA/UDMH propellants.

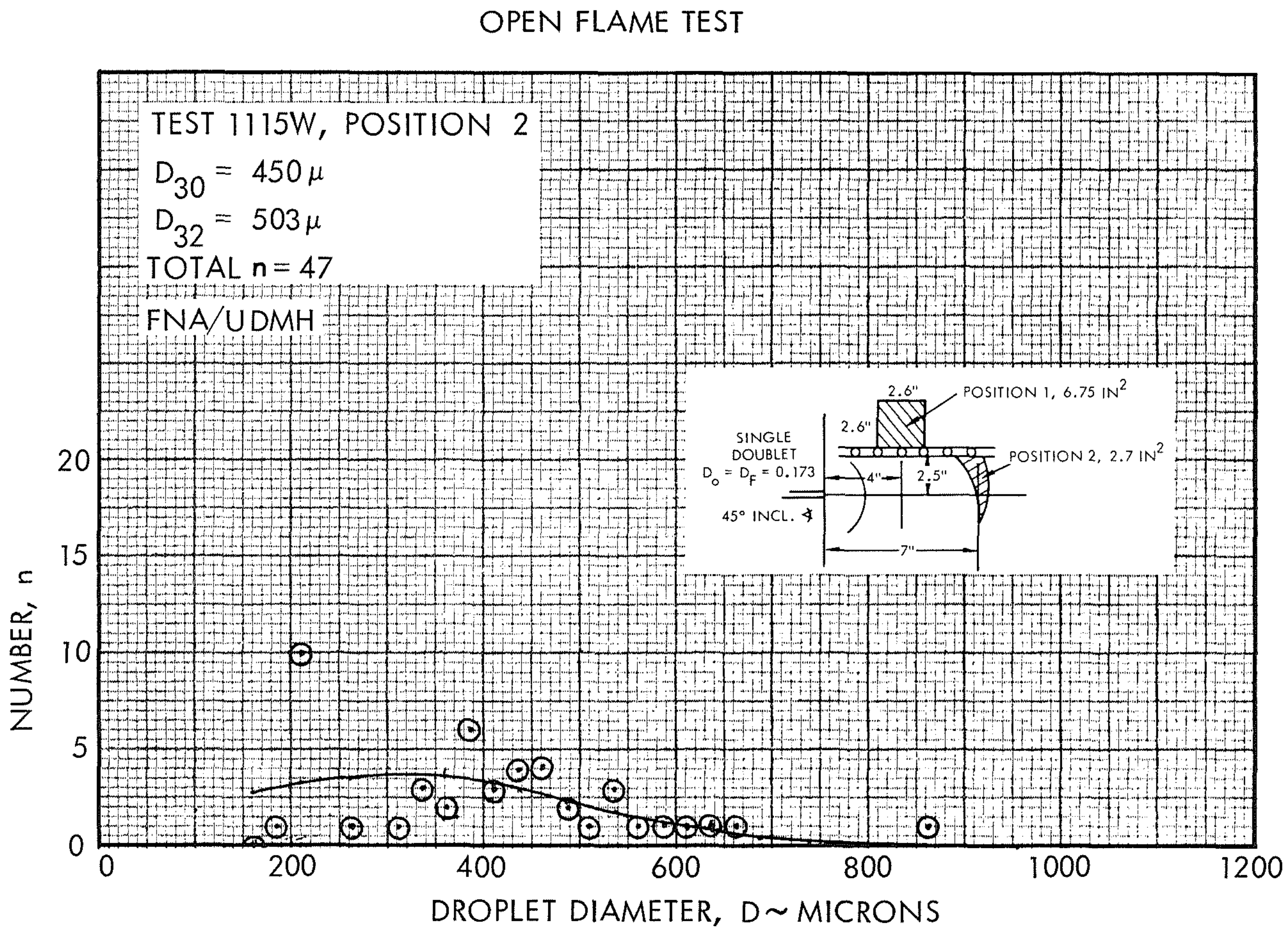

Figure 28. Experimental droplet count in 25 micron interval versus droplet diameter for open flame test B1115W, position 2, with FNA/UDMH propellants.

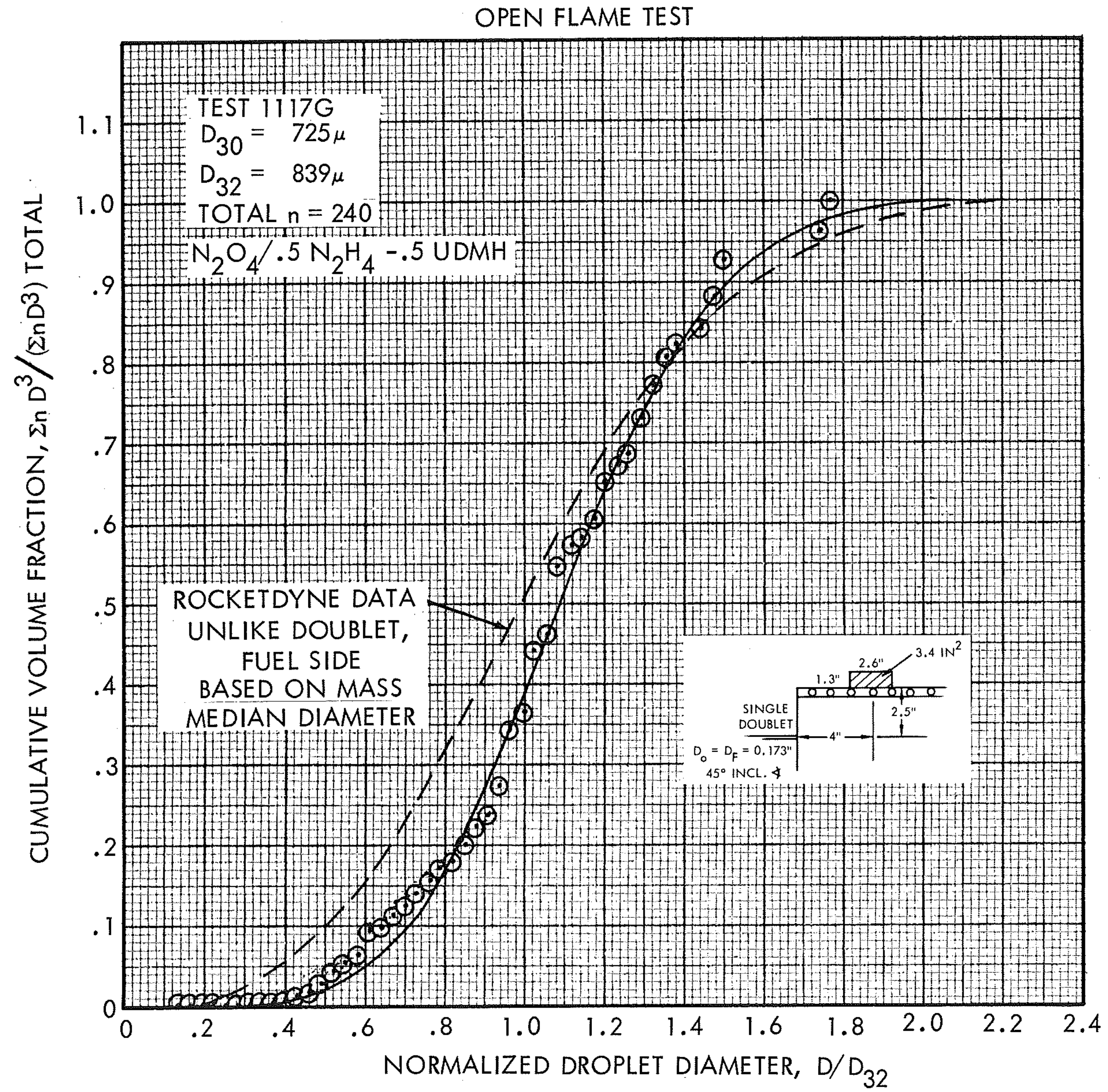

Figure 29. Experimental cumulative volume fraction versus normalized droplet diameter for open flame test B1117G, with $N_2O_4/.5\ N_2H_4-.5$ UDMH propellants.

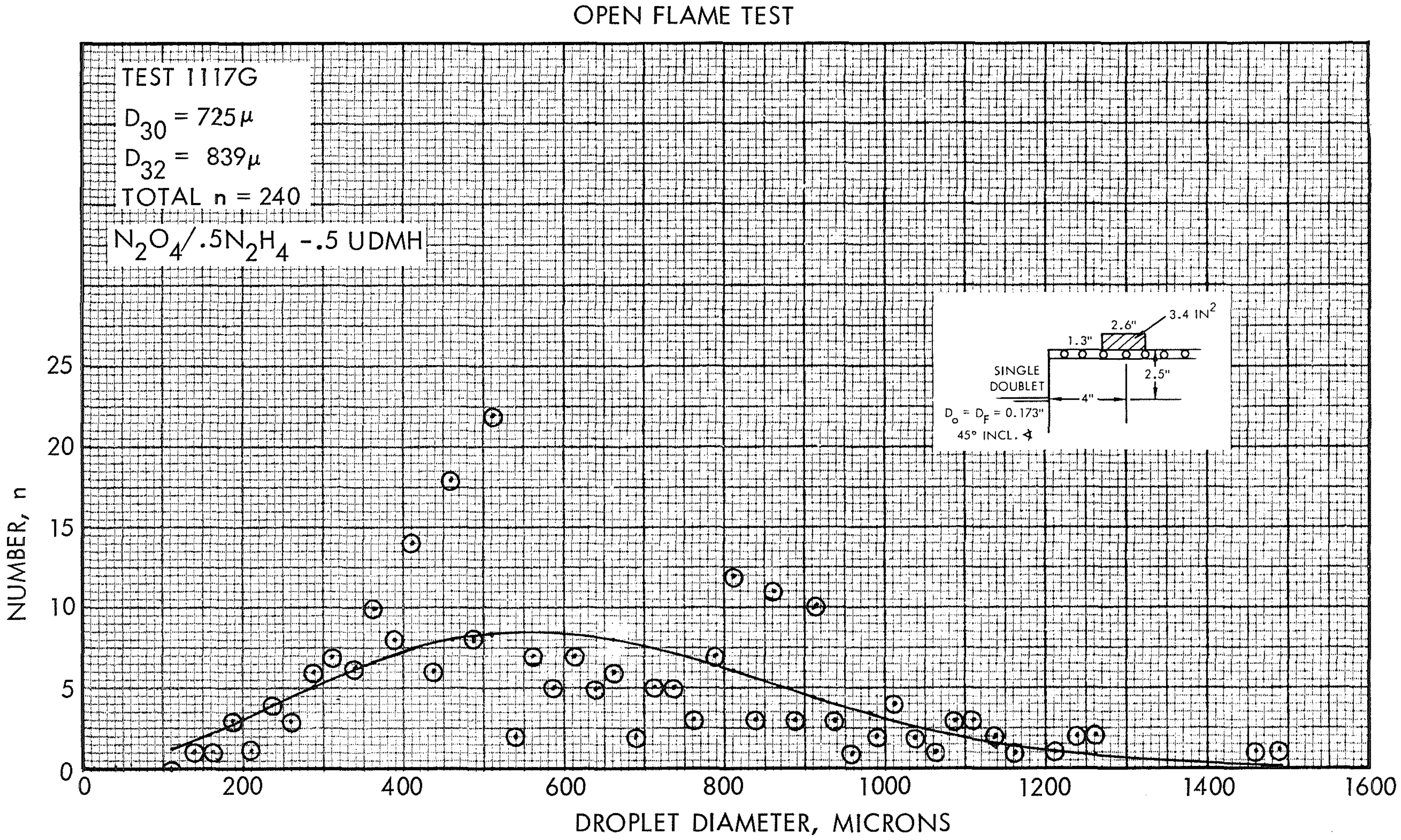

Figure 30. Experimental droplet count in 25 micron interval versus droplet diameter for open flame test B1117G, with $N_2O_4/.5\ N_2H_4-.5$ UDMH propellants.

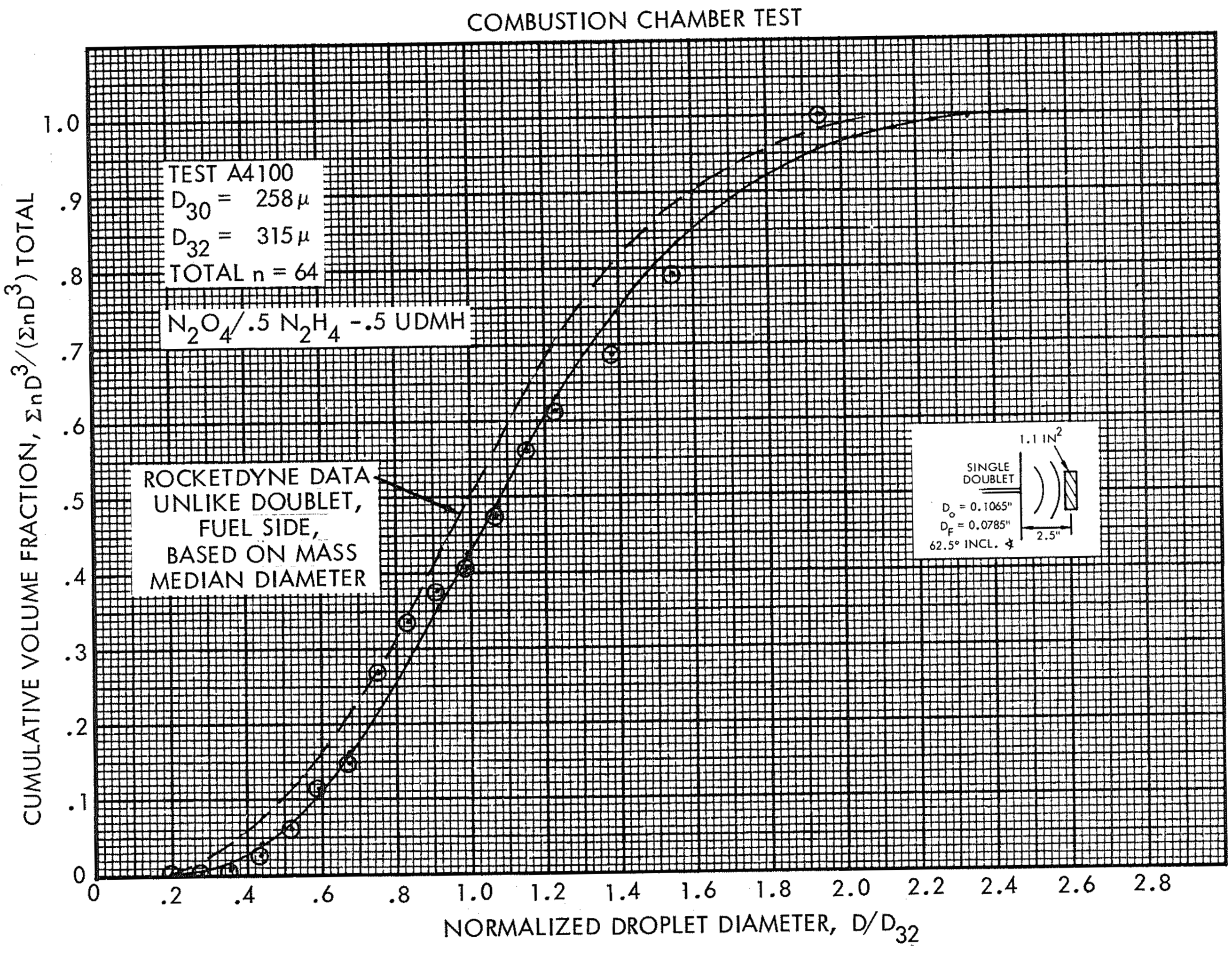

Figure 31. Experimental cumulative volume fraction versus normalized droplet diameter for combustion chamber test A4100, with N_2O_4/ 5 N_2H_4-.5 UDMH propellants.

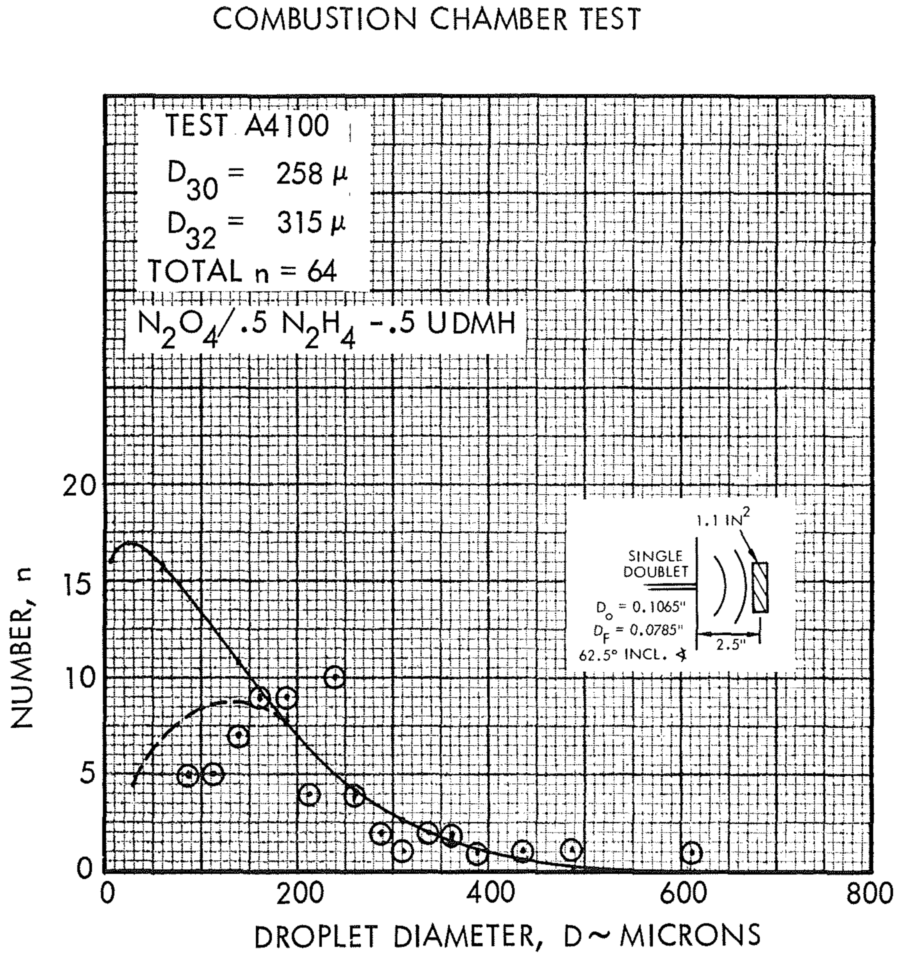

Figure 32. Experimental droplet count in 25 micron interval versus droplet diameter for combustion chamber test A4100, with N_2O_4/.5 N_2H_4-.5 UDMH propellants.

flow test. Although the population consisted of only 47 droplets for Position 2 (7 inches downstream of impingement along the jet element centerline), the measured D_{32} of 503 microns was within 10 percent of D_{32} of 465 microns for the larger population measured in Position 1, which is 4 inches downstream of impingement and 2-1/2 inches or more from the jet element centerline. The D_{32} of 839 microns measured for the open flame Test B1117G with $N_2O_4/0.5N_2H_4$-0.5 UDMH is considerably higher than the value of 465 microns measured near the same position for Test B1115W, with RFNA/UDMH. The higher value apparently results from the higher surface tension of 0.5 N_2H_4-0.5 UDMH compared to UDMH, as discussed in Section 3.1.

Photographs of the open flame sprays for Tests B1115W and B1117G were shown in Figures 9 and 10. The very dense spray in the center regions apparently obscured the droplets in these regions with the holographic equipment used. Thus, substantial numbers of drops were visible only in the peripheral regions, where the droplet counts were made.

A typical reconstruction photograph for Test B1157 with the 3-inch-diameter acrylic chamber was seen in Figure 13. The dense liquid fan region terminates approximately 1-1/2 inches downstream and changes to a "lacy" structure of combustion material. Although Figure 33 is not of the combustion phenomena recorded for Test B1157, it does serve to illustrate some typical lacy structure observed in nearly all of the combustion holograms (both open flame and, to a greater extent, in the 3-inch-diameter chamber tests) recorded during the original program. The illustrations of Figure 33 show three photomicrographs of small portions of the combusting N_2O_4 and 50/50 N_2H_4-UDMH spray recorded during open flame Test B1117G (refer also to Figure 10). Note the difficulty in discerning specific droplets and, further, assigning an equivalent diameter to selected droplets.

Study of negatives and positives of 20 holographic reconstructions under various magnification for Test B1157 and similar Test B1149 and B1162, revealed that the lacy structure appears as light and dark granular regions. The size of the granularity which is the same color as the droplets is equivalent to a D_{32} of 55 microns. A measurement of a sample of 100 was made in the lacy structure region located in Figure 20

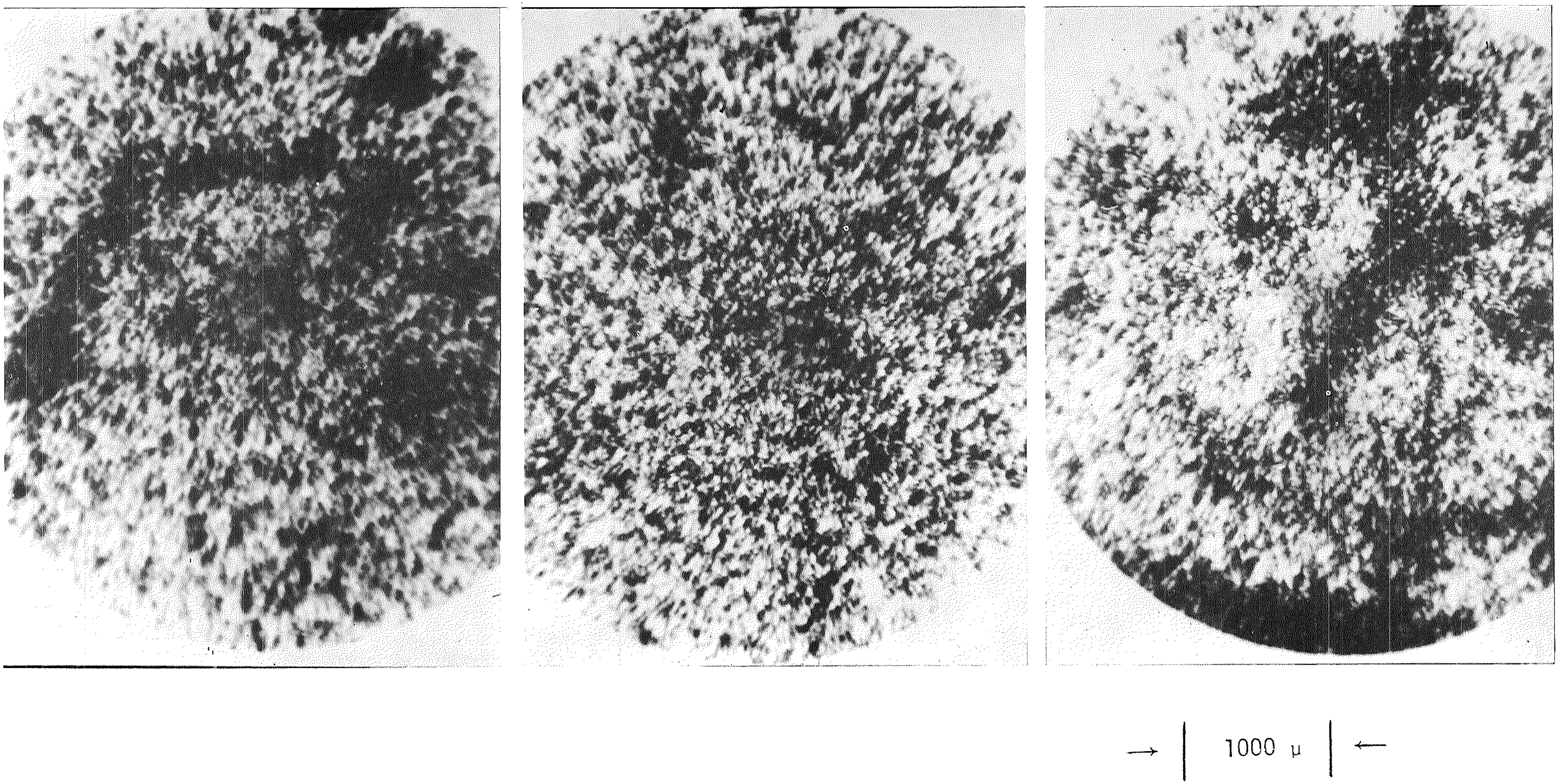

Figure 33. Three photomicrographs of portions of a SO243 photograph of the reconstruction of pulsed ruby laser Hologram B1117G of open flame combustion. The hologram was originally recorded on 2-6-68 at JPL-Edwards of N_2O_4 - 50/50 N_2H_4· UDMH propellant combustion.

because it was not clear at the time if the small measurements were droplets or background granularity. (The number-diameter distribution for the measurements is presented subsequently in Figure 34.) The conclusion is made that the measurements with photographs of Test B1157 holographic reconstructions are background granularity. Liquid droplets are not distinguishable. Study of the holographic reconstruction of a comparable USAF 1951 resolution chart indicated that the smallest element which could be distinguished was Column 3, Row 1 which corresponds to a background size or resolution of approximately 60 microns, which substantiates the conclusion.*

In lieu of droplet measurements from Test B1157, a hologram reconstruction was selected from more recent work under Air Force sponsorship Reference 7 which used improved holographic equipment and techniques. Droplet measurement results for the Air Force Test A4-100 are presented in Table II and Figures 31 and 32. All droplets were counted in a single plane region, 1.1 in^2, a distance of 2.5 inches downstream of impingement about the centerline of the injection element. Even though a very limited droplet population of 64 was discernible, the cumulative distribution is quite similar to those for both the water flow and open flame tests.

---

*Refer to Appendix A for an explanation of this USAF 1951 resolution target.

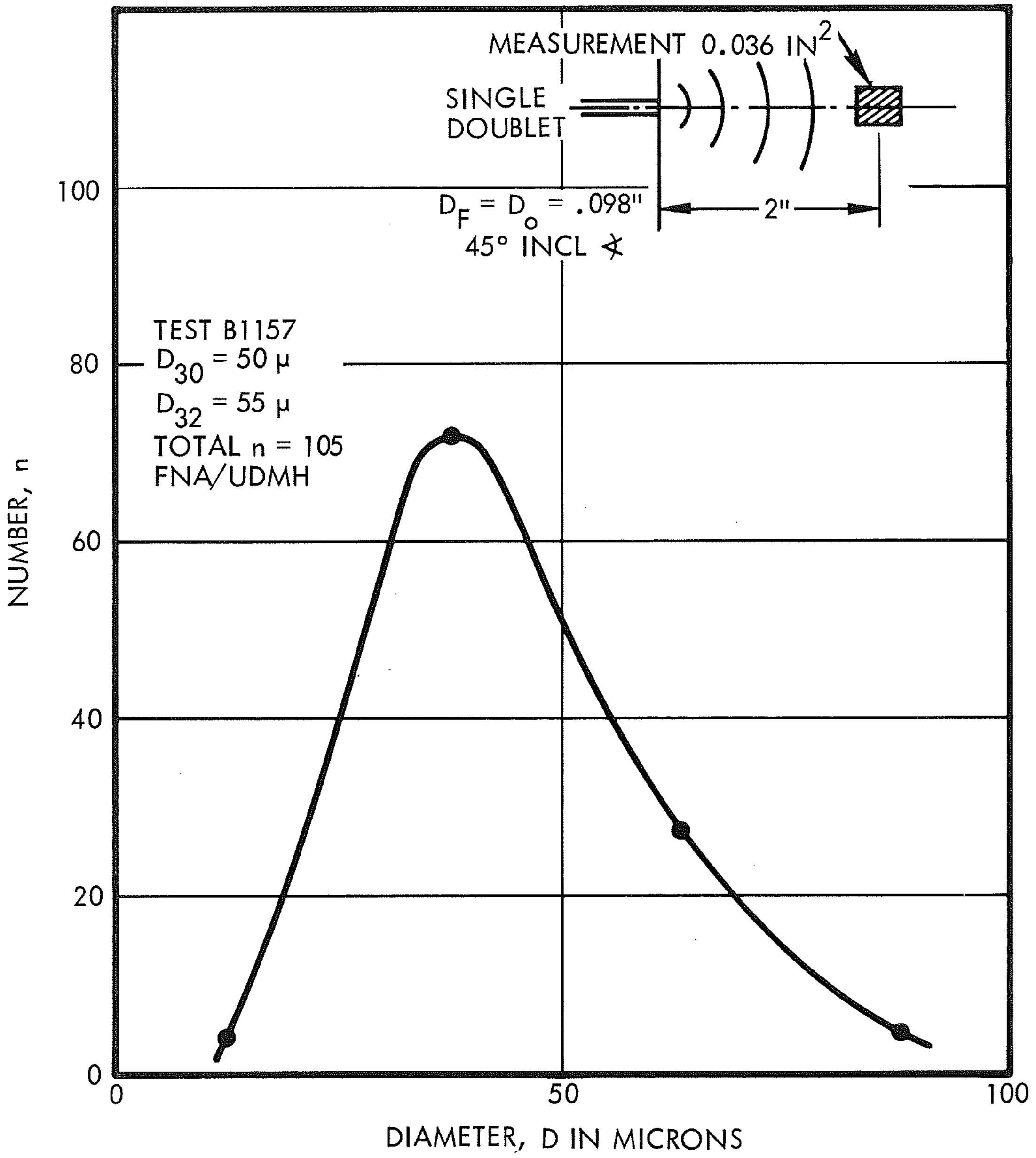

Figure 34. Background granularity size distribution for combustion chamber test B1157, for a 25 micron interval

3. DISCUSSION OF RESULTS

3.1 COMPARISON WITH MEAN DROPLET DIAMETER CORRELATIONS

Although a considerable number of empirical mean droplet correlations have been developed, based on droplet measurement with various spray devices and atomizers, very few correlations have been reported for two impinging liquid streams at included angles of 90 degrees or less. Two correlations, Ingebo's (Reference 8), and Rocketdyne's (Reference 9) will be used for comparison. The Ingebo correlation is:

$$\frac{D_j}{D_{30}} = 2.64 \sqrt{D_j V_j} + 0.97 D_j \left| V_{air} - V_j \right| \qquad (3)$$

where D_j has units of inches and V has units of ft/sec. The Ingebo correlation is derived from cold flow tests with two impinging streams of heptane, at a 90-degree included angle, into a large diameter air stream moving in the same direction. The droplet diameters were measured from photomicrographs of the spray 8 inches downstream of impingement. Approximately 1400 drop images were measured for each test condition, which resulted in a reported statistical error-factor of approximately 3.5 percent. The maximum observed droplet diameter was 1160 microns. The volume mean drop diameter is defined as

$$D_{30} = \left(\frac{\Sigma n_i D_i^3}{\Sigma n_i} \right)^{1/3} \qquad (4)$$

The correlations reported by Rocketdyne are based on the freezing, sieving and weighing of hot wax injected through one or more impinging jets into still air. For impingement of two hot wax jets (orifice L/D = 10) of equal diameter at a 60 degree included angle, the empirical correlation for the mass median diameter, $\bar{D}$, is

$$\bar{D} = 7.84 \times 10^4 \left(\frac{D_j^{0.57}}{V_j^{0.85}} \right) \qquad (5)$$

where $\overline{D}$ has units of microns, D_j is in inches and V_j is in ft/sec. The mass median diameter is that diameter below which is contained 50 percent by weight of the droplets. The injection element represented by Equation 5 is termed a like doublet with infinite spacing by Rocketdyne. For impingement of one hot wax jet on one water jet of unequal diameters at an included angle of 60 degrees, the empirical correlation for mass median diameter, $\overline{D}$, for the wax jet, which represents the fuel side, is

$$\overline{D} = 9.95 \times 10^{4} \left[\frac{D_F^{\,0.27} \; D_o^{\,0.023}}{V_F^{\,0.74} \; V_o^{\,0.33}} \right] \qquad (6)$$

The Ingebo and Rocketdyne correlations apply only to heptane and liquid wax, respectively, at the respective impingement angles and must be corrected for physical property effects. The effect of liquid physical properties on drop size (Ref. 9) is approximately

$$\frac{D}{D_o} = \frac{\mu^{1/3}\;{}^{1/2}}{\rho^{1/6}} \bigg/ \frac{\mu_o^{1/3}\,\sigma_o^{1/2}}{\rho_o^{1/6}} \qquad (7)$$

It is to be noted that there is considerable disagreement on the powers assigned to the liquid properties among the available models. Physical properties of water, UDMH, 0.5 N_2H_4-0.5 UDMH and heptane are listed in Table III. The differences in surface tension, σ_L, have the most pronounced effect. The correction factor for physical properties by which the mean diameters computed from the Ingebo and Rocketdyne corrections are to be multiplied are listed in Table IV.

Very little has been reported on the effect of the included angle on mean droplet diameter. Dombrowski and Hooper have reported that for constant diameter jets of water for fully developed turbulent flow

$$D_{30} \sim \frac{1}{(\sin\theta)^{1.16}} \qquad (8)$$

where θ is one-half of the included angle (Reference 10).

The measured and predicted values of mean droplet diameters are compared in Table II with corrections made for liquid physical properties and, as noted, for impingement included angle. Air-to-jet velocity difference of 0 and V_j are used with the Ingebo correlation. Ingebo 8 uses $V_{air} - V_j = V_j$ for injection into still air. The velocity difference is commonly taken as zero for estimation of drop sizes in liquid propellant rocket combustion chambers, with the assumption that the velocities of the evolving combustion chamber gases is approximately equal to the injected liquid velocity. Use of the Ingebo correlation for the water flow test results in a low predicted value of D_{30} for $\Delta V = V_j$, 90 degree impingement. The most probable cause of the large measured mean diameter is the low 45 degree impingement angle. If the Ingebo correlation is modified by Equation 8, the predicted D_{30} at $\Delta V = V_j$ for the water flow test is

$$D_{30} = 343 \left[\frac{\sin 90/2}{\sin 45/2}\right]^{1.16} = (343)(2.04) = 700 \qquad (9)$$

This correction results in a predicted value of D_{30} which is very nearly the same as measured at Position 1 for the water flow test.

Modification of the Ingebo prediction for $\Delta V = V_j$ for the impingement angle correction for the open flame tests results in predicted values of D_{30} which are somewhat less than the measured values. The more significant measured mean drop diameters were obtained in a region considerably removed from the center line of the spray fan. Blow-apart of the reactive streams may have contributed to the higher measured value of D_{30}. The experimental conditions for both open flame tests were such that Rupe's criterion for optimum mixing for an unlike doublet (Reference 11)

$$(\rho V_j^2 D_j)_o \Big/ (\rho V_j^2 D_j)_f - 1.0 \qquad (10)$$

was approximately met. The right hand side of Equation (10) is 0.95 for Tests B1115W and B1117G. The predicted value of D_{30} $\Delta V = V_j$, corrected for physical properties and impingement angle, is considerably larger than that measured for the combustion chamber Test A4-100. The high temperature combustion environment probably accounts for the smaller measured D_{30}. The use of $\Delta V = V_j$ for the combustion chamber test is considered appropriate because of the low combustion performance and,

Table III. Liquid Physical Properties ($T = 60^{o}F$)

	Water	UDMH	$.5N_2H_4$— .5UDMH	Heptane
Surface Tension, $L \frac{\text{dyne}}{\text{cm}}$	72	24	45.4	19.7
Viscosity, $\mu_L \frac{lb_m}{\text{sec ft}}$	7.5×10^{-4}	4.2×10^{-4}	6.35×10^{-4}	2.60×10^{-4}
Density, $\rho_L \frac{lb_m}{ft^3}$	62.4	50.0	56.6	42.7

Table IV. Mean Drop Size Correction Factors for Physical Properties

	Ingebo (Heptane)	Rocketdyne (Wax)
H_2O	2.47	1.133
UDMH	1.30	0.594
$.5N_2H_4$-.5UDMH	1.70	0.782

therefore, low initial combustion gas velocity. However, for combustion chamber Test A4-100, for which the injector included angle is approximately the same as used for the Rocketdyne tests, the experimental value of volumetric median diameter is very nearly the same as that predicted by the Rocketdyne correlation.

The differences in drop size between the open flame tests is attributed to differences in physical properties of the two fuels since the same injector was used and injection velocities were nearly identical. The predicted larger mean drop size ratio with 0.5 N_2H_4-0.5 UDMH to that with UDMH of 1.31 from Equation 7 is somewhat less that the measured value of 1.75, based on D_{30}. It is assumed that the droplets measured are fuel droplets because the oxidizers vaporize at much lower temperature than the fuels at the same pressure. The higher surface tension of 0.5 N_2H_4-0.5 UDMH primarily accounts for the larger mean drop size. The drop size correction factors for the open flame tests are based on physical property data for viscosity and density at the fuel temperatures used at the test conditions. However, the surface tension of 0.5 UDMH-0.5 N_2H_4 was computed from the average of that for N_2H_4 (66.7 dyne/cm) and UDMH (24 dyne/cm) at 60°F, for lack of better data.

For the water flow test, the experimental value of volume median or mass median diameter is 12 percent larger than the experimental value of D_{32}, and 44 percent larger than the experimental value of D_{30}. For the open flame and combustion tests the mass median diameter exceeds D_{32} by 2 to 12 percent and exceeds D_{30} by 18 to 37 percent.

3.2 COMPARISON WITH DROPLET SIZE DISTRIBUTIONS

The cumulative mass fraction versus $D/\bar{D}$ from the normalized Rocketdyne experimental data (Reference 9) is compared with the holographic data reduction of cumulative volume fraction versus D/D_{32} for each test. (Figures 21, 23, 25, 27, 29, and 31). If the experimental data is normalized using the volumetric or mass median diameter, $\bar{D}$, by shifting the experimental curves to the left by a constant multiplication factor, such that at the cumulative volume fraction of 0.5 the normalized droplet diameter is 1, the experimental data would more closely match the Rocketdyne experimental data. However, the very similar characteristic between the two different sets of data is evident in the manner presented, even though the droplet populations from the holographic reconstruction measurements are limited.

To obtain completed droplet populations with the holographic technique such as that obtained by freezing, sieving and weighing a segment of the wax spray volumetric flow would require droplet measurements with holographic reconstructions at different planes across the non-reactive spray. This can be accomplished and mechanized techniques can be developed for droplet measurements to reduce the cost of data analysis. The holographic technique is the only known method by which droplet size distribution can be obtained for a volume segment of the flow at different axial station in a combustion environment. However, for the limited droplet population data which is available, the precision of the measurements and confidence in the local mean droplet sizes and distributions is an important consideration. This is discussed in Section 3.4.

The cumulative volume distribution for the water flow tests relatively closely matches the Rocketdyne data for the like doublet at cumulative volume fractions less than 0.5. The small number of large diameter drops which were measured significantly affects the shape of the distribution and tends to distort the cumulative volume fraction from a smooth curve at the higher values. The cumulative volume fraction for the open flame tests compares closer to the Rocketdyne like doublet data than to the unlike doublet data. The experimental data was obtained with equal diameter fuel and oxidizer orifices, just as for the like doublet, whereas the Rocketdyne unlike doublet data was obtained with fuel and oxidizer orifices of unequal diameter.

The curves drawn through the cumulative distributions are based on a curve fitting and the General Exponential size distribution to the cumulative data, expressed in terms of $n_iD_i^3$ and D_i/D_{32}. The General Exponential function 12 is:

$$\frac{d}{dx}\left[\Sigma n_iD_i^3/(\Sigma n_iD_i^3)_{total}\right] = UX^C \exp\left[-BX^A\right] \qquad (11)$$

where $X = D/D_{32}$ and U, C, B, and A are constants. The General Exponential function was found to provide the best fit to the Rocketdyne data, compared to the Rosin-Rammler, Nukiyama-Tanasawa, Log Probability and Upper Limit distributions which are also commonly used to fit droplet distribution data. The curve fits were obtained by integrating Equation (11) and in-putting this equation and the cumulative $n_i D_i^3$ data and the D_i/D_{32} data to an available computer program which iterated the selected initial values of the constants until the sum for all test data of the squares of the differences between the cumulative data points and the curve ordinates fell below specified levels. This "miss" varied from 0.01 to 0.07 for the tests. The values of the constants and the sum of the squares of the differences are listed in Table V for each test. Comparison of the curves with the data points on the cumulative distribution curves indicates that the General Exponential function provides a very close fit to the experimental data.

No curve fit is shown for water flow Test B 1113W, Position 2. The large diameter drops which were counted resulted in an abrupt termination of the "S" curve for this test. The general exponential function will not fit this condition without disregarding several of the upper end data points.

The curve through the number-diameter data for each test is obtained by substituting the constants into Equation (11). The number of droplets in a diameter interval of 25 microns is obtained from

$$n_i = \left\{ \frac{\Delta \left[\Sigma n_i D_i^3 / \left(\Sigma n_i D_i^3 \right) \text{ Total} \right]}{\Delta x} \right\} \frac{\left(\Sigma n_i D_i^3 \right) \text{Total}}{D_i^3} \quad \frac{25}{D_{32}} \qquad (12)$$

where $\Delta x = 25/D_{32}$. The curves for the number-diameter data are thus consistent with the cumulative distribution curves. The curves representing the n_i - D_i data are proportional to the magnitude of the slopes of the cumulative distribution curves. The low end of each cumulative distribution curve is actually not closely fit to the data, in terms of percent difference in local value of the slope; therefore, some of the n_i - D_i curves as drawn at lower D_i values are clearly not representative of the data. The dashed lines in Figure 22, 26, and 32 are based on a closer fit of the lower end of the cumulative distribution data and thus appear more representative of the n_i - D_i data. However, the solid line curves result in lower values of the sums of the squares of the differences between the curves and data for the cumulative distributions. The curve fits are based

Table V. General Exponential Curve Fit Constants for Cumulative Volume Fraction

TEST	POSITION	TOTAL COUNT	U	C	B	A	$\sum_{i}^{N}(Y_{data} - Y_{curve})^2$
B1113W	2	495	-	-	-	-	
B1113W	1	179	4.960	2.716	1.800	1.500	0.023
B1113W	1	146	4.493	-3.465	1.666	-1.582	0.070
B1115W	1	218	7.148	3.833	1.823	2.088	0.012
B1115W	2	47	4.27	3.825	1.149	3.036	0.011
B1117G		240	7.253	4.623	1.780	2.269	0.019
A4-100		64	7.557	3.069	2.127	1.503	0.018

$$Y = \Sigma n_i D_i^3 / (\Sigma n_i D_i^3)\ \text{total}$$

on use of a unimodal distribution function. The number-diameter data for the open flame test indicates that the test data may actually be bimodal, which could result from secondary atomization.[12] The actual size distribution may be a composite of various individual size distributions. More extensive data would be required to warrant curve fitting with multimodal distribution functions.

3.3 COMBUSTION MODELING

An important use of the combustion holographic technique is to measure droplet size distributions at several different axial locations along the combustion chamber. The mean droplet sizes determined experimentally can then be compared to those predicted from available combustion models for refinement of the models under different operating conditions. The limited combustion holographic data available do not include measurement of mean droplet variation along the chamber axis. However, a combustion model was used to predict the droplet size variation and combustion performance along the chamber axis for Test Run A4-100. This was subsequently compared with the mean droplet diameter determined at one axial location in the chamber and the experimental C* efficiency for this run using a single element unlike doublet injector. The measured D_{30} droplet diameter and combustion efficiency for Test A4-100 were approximately 258 microns and 62 percent, respectively.

The steady-state, one-dimensional, vaporization rate-limited program described in Reference 8 was employed to calculate the D_{30} variation with chamber length. The results are presented in Figure 35 as D_{30} versus axial chamber length. Figure 35 also shows the total propellant vaporized as a function of combustion chamber length. The origin of the vaporization process is the impingement point of the single element unlike doublet injector. The impingement distance was approximately 0.30 inch downstream of the chamber head end (injector face) as shown in the plot of Figure 35.

The referenced program predicted a gradual decrease in the mean droplet diameter with increasing chamber length for the test operating conditions of the A4-100 firing. Correspondingly, only about one-third of the total propellant was vaporized after six inches of combustion length. These analytically predicted results must be compared with the measured

C^* efficiency of ~62 percent and the measured D_{30} value of 258 microns 2.5 inches downstream of the injector face. At variance with the experimental combustion efficiency is the vaporization model C^* prediction of approximately 40 percent.

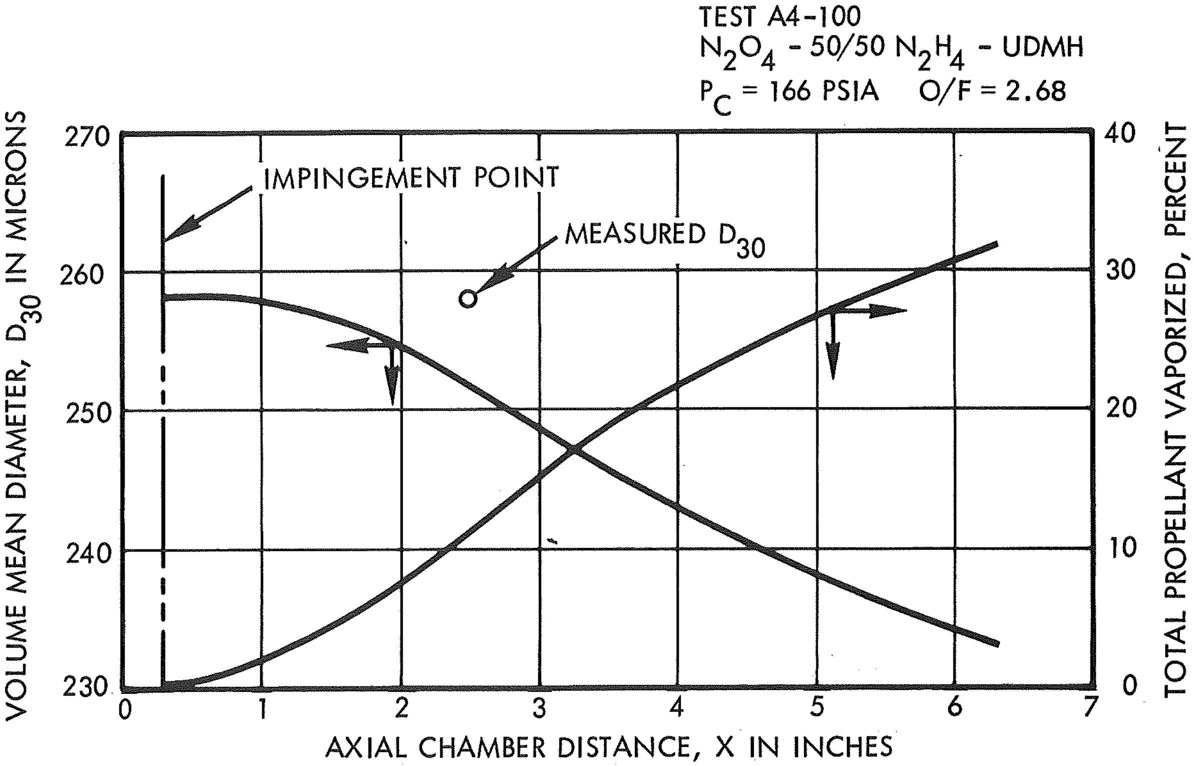

Figure 35. Predicted variation of volume mean droplet diameter along combustion chamber. The holographic measurements were made 2.5 inches downstream of the injector face.

This brief attempt to compare measured drop size information and combustion performance with an existing analytical model has not yielded conclusive results. There is insufficient holographically derived data available to describe changes in mean droplet diameter over the length of the combustion chamber volume.

3.4 MEASUREMENT ERROR ANALYSIS

The droplets on both negative or positive film as seen through a microscope at 15 or 30 magnification are, for the most part, not circular nor do they possess sharply-defined boundaries for the water flow, open flame and combustion chamber tests. An equivalent diameter was estimated for each droplet using the measuring microscope, which can be read to within 0.0001 inch. The uncertainty in the measurement of the larger drops is primarily in estimation of the equivalent diameter, whereas the uncertainty in measurement of the smaller droplets results from the fuzzy boundaries which make up a significant percent of the equivalent droplet diameters. By repeated measurements on individual droplets, it is estimated that the uncertainty in measurement of each droplet in the flow field regions which were selected for data reduction averages approximately ±10 percent. The effect of this uncertainty in measurement is as follows for D_{32}

$$D_{32} = \frac{\Sigma n\, D^3}{\Sigma n\, D^2}$$

Differentiating D_{32}, replacing the differentials by incrementals and dividing by D_{32} results in

$$\frac{\Delta D_{32}}{D_{32}} = \frac{\Delta \Sigma n D^3}{\Sigma n D^3} - \frac{\Delta \Sigma n D^2}{\Sigma n D^2} \qquad (13)$$

For droplet measurements of D ± xD, the incrementals can be expressed as

$$\Delta\Sigma nD^3 = \left(n_1D_1{}^3 + n_2D_2{}^3 + \cdots\right) - \left[n_1\left(D_1 \pm xD_1\right)^3 + n_2\left(D_2 \pm xD_2\right)^3 + \cdots\right]$$

$$= \left(n_1D_1{}^3 + n_2D_2{}^3 + \cdots\right) - \left[n_1D_1{}^3 (1 \pm x)^3 + n_2D_2{}^3 (1 \pm x)^3 + \cdots\right]$$

$$= n_1D_1{}^3\left[1 - (1 \pm x)^3\right] + n_2D_2{}^3\left[1 - (1 \pm x)^3\right]$$

$$= \left[1 - (1 \pm x)^3\right]\Sigma nD^3 \tag{14}$$

Similarly, for $\Delta\Sigma nD^2$

$$\Delta\Sigma nD^2 = \left[1 - (1 \pm x)^2\right]\Sigma nD^2 \tag{15}$$

Substituting in Equation (13)

$$\frac{\Delta D_{32}}{D_{32}} = 1 - (1 \pm x)^3 - \left[1 - (1 \pm x)^2\right] = \pm x\ (1 \pm x)^2 \tag{16}$$

The maximum uncertainty, if one observer read all measurements +10 percent high, would be

$$\frac{\Delta D_{32}}{D_{32}} = +\,0.10(1.10)^2 = +\,0.121$$

If the observer made all measurements 10 percent low, the effect on D_{32} would be

$$\frac{\Delta D_{32}}{D_{32}} = -\,0.10(0.90)^2 = -\,0.081$$

Thus, if the droplets can be measured to within ±10 percent, the maximum variation which could occur in D_{32} would be +12 percent or -8 percent. Since most observers will make single measurements which are in some cases too high and in some cases too low compared to the mean of repeated readings of a number of observers, it is more representative if the variations are expressed in terms of the standard deviation, σ. For equivalent droplet diameter measurements of D ± 0.1D, if 0.1 D is considered to be 2 times the standard deviation (0.95 percent confidence level), the estimated odds are that the true value of the droplet diameter falls within the range of D ± 0.1D are 20 to 1.

For D_{32}

$$\sigma_{D_{32}} = \left(\frac{d\,D_{32}}{dD} \quad \sigma_D \right)^2 \tag{17}$$

$$\frac{d\,D_{32}}{dD} = \frac{d}{dD} (\Sigma nD^3/\Sigma nD^2) = \frac{(\Sigma nD^2)(3)(\Sigma nD^2) - (\Sigma nD^3)(2)(\Sigma nD)}{\left(\Sigma nD^2\right)^2}$$

$$= 3 - 2\,D_{32} \frac{\Sigma nD}{\Sigma nD^2} = 3 - 2 \frac{D_{32}}{D_{21}} \tag{18}$$

From experimental results for Run B1113W for a droplet count of 146 the measured D_{32} and D_{21} are 893 microns and 787 microns, respectively. Therefore,

$$\sigma_{D_{32}} = \left[3 - 2 \left(\frac{893}{787} \right) \right] \sigma_D = 0.73\,\sigma_D$$

The standard deviation of D_{32} is approximately three-fourths of the standard deviation of the individual droplets. The true value of D_{32}, for the regions analyzed, therefore should be within ±7.5 percent of the measured values at the 95 percent confidence level. Measurements of two different observers for the same region of the reconstructed hologram for the water flow test (B1113W) resulted in a difference in D_{32} of approximately 5 percent. The standard deviation for two measurements with equal variances (σ_{mD}) is

$$\frac{1}{\sigma_{mD}^2} = \sum^{2} \frac{1}{\sigma_D^2} = \frac{2}{\sigma_D^2}$$

$$\sigma_{mD} = \sigma_D/1.414$$

The true value of D_{32} should fall within ± (0.73/1.414) 100 or approximately ±5 percent of the mean of the measured value for Test B1113W of 918 microns for the region measured, at the 95 percent confidence level.

Least squares curves of the general exponential distribution function were fitted to the cumulative distribution of the basic holographic particle size data sets.

Mathematically the fitted function was of the form

$$Y = UX^C e^{-BX^A}$$

where

X = normalized droplet diameter, D/D_{32}

Y = cumulative volume fraction

The errors of fit for the various data sets are presented in Table VI.

It is obvious from this table that the error standard deviation estimates are reasonably consistent. Thus a pooled estimate of the error was calculated. It will be noted that the 95 percent confidence interval for this overall pooled estimate is narrower than any of the individual intervals. This, of course, is due to the increased precision made possible by using the total sample size.

Data sets for Test B1113W were actually the same holographic reconstruction photograph read by two different readers. The two individual errors are both seen to be consistent with the hypothesis of a single overall standard deviation.

Table VI. Particle Error Analysis

N No. of Data Intervals	Total Particle Count	$\sum(y-y^2)$	s_e^2	s_e (percent)	95 Percent Confidence Interval for (percent)
22	47	0.0109	0.00061	2.5	1.9 - 3.7
48	240	0.0185	0.00042	2.0	1.6 - 2.5
24	218	0.0118	0.00059	2.4	1.8 - 3.5
17	64	0.0137	0.00105	3.2	2.3 - 5.2
38	146	0.0268	0.00079	2.8	2.3 - 3.7
47	179	0.0231	0.00054	2.3	1.9 - 2.9
85	325	0.0500	0.00062	2.5	2.2 - 3.0
				s_e(pooled) = 2.5	2.2 - 2.8

(s_e = Standard deviation of the error)

The number of droplet diameters which were measured for each test is small, relative to other experimental techniques which have been reported in the literature. It is significant, therefore, to estimate the confidence in the results which can be obtained with small droplet counts compared to larger counts.

Table VII shows the effect of sample size on increasing the confidence for the 10th, 50th and 90th percentiles of a cumulative distribution function, with parameters as defined in Figure 36.

Table VII

n	$P(\hat{x}_{.05} < x_{.10} < \hat{x}_{.15})$ $= P(\hat{x}_{.85} < x_{.90} < \hat{x}_{.95})$	$P(\hat{x}_{.45} < x_{.50} < \hat{x}_{.55})$
20	.56	.34
40	.71	.47
100	.91	.68
200	.99	.84
300	.996	.92

The probability that the true population percentile, x_p, of a cumulative distribution will lie within a sample interval of $(\hat{x}_{p-.05}, \hat{x}_{p+.05})$ is tabulated.

The table is based on a Walsh method (Reference 14) for obtaining non-parametric confidence intervals for percentiles of continuous cumulative distribution functions.

It is thus seen that the confidence probability increases rapidly as sample size increases from 20 to 300.

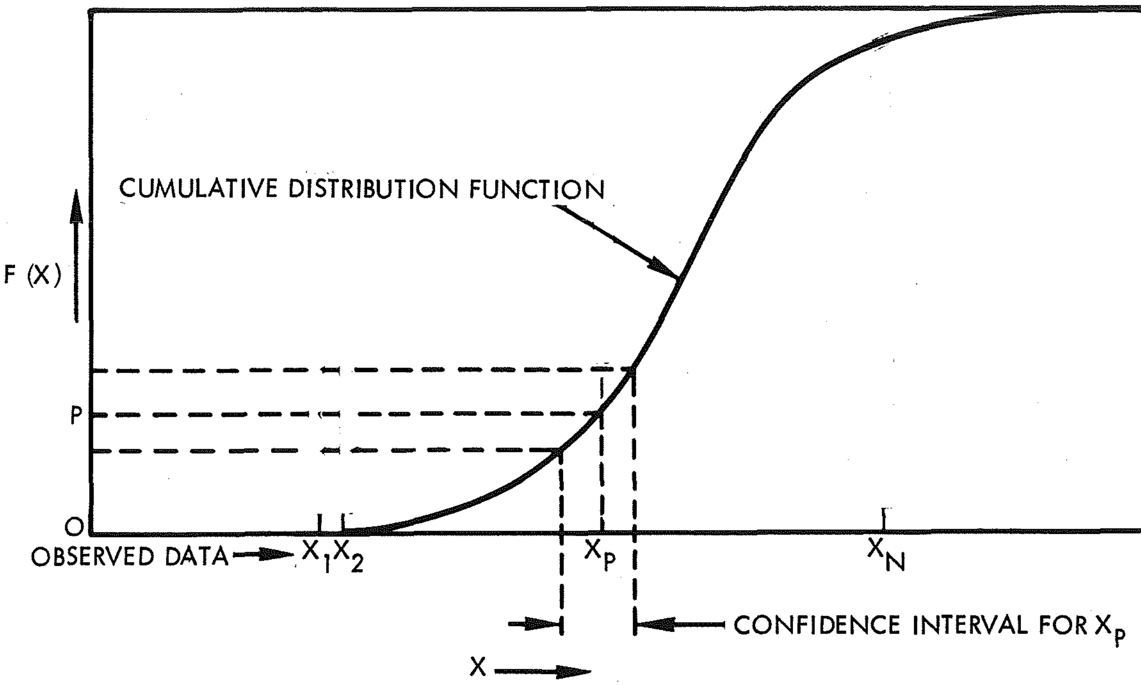

F(X) IS THE CUMULATIVE DISTRIBUTION OF PARAMETER X

$X_1, X_2, \ldots\ldots X_N$ ARE THE ORDERED VALUES OF THE SAMPLED OBSERVATIONS

X_P IS THE PTH PERCENTILE OF F(X)

X_P IS A SAMPLED ESTIMATE OF X_P

Figure 36. Effect of sample size on confidence intervals for cumulative distribution percentiles.

Applying the method to the water flow test data in Figure 21, as an example, the estimated 45th and 55th percentiles are drawn in and projected down to the x-axis where the corresponding values of normalized droplet diameter are determined to be about 1.06 and 1.18, respectively (See Figure 37). Next, interpolating in Table VII for the n = 146 of observer 1, the probability is determined to be about .75 that the true population 50th percentile would lie between a 1.06 and 1.18 normalized droplet diameter. The corresponding probability for observer 2 which had a sample size of 179 is similarly interpolated to yield approximately 0.80. From Table VII it is also seen that these probabilities could both be increased to 0.92 if the particle count could be increased to n = 300, for example.

WATER FLOW TEST

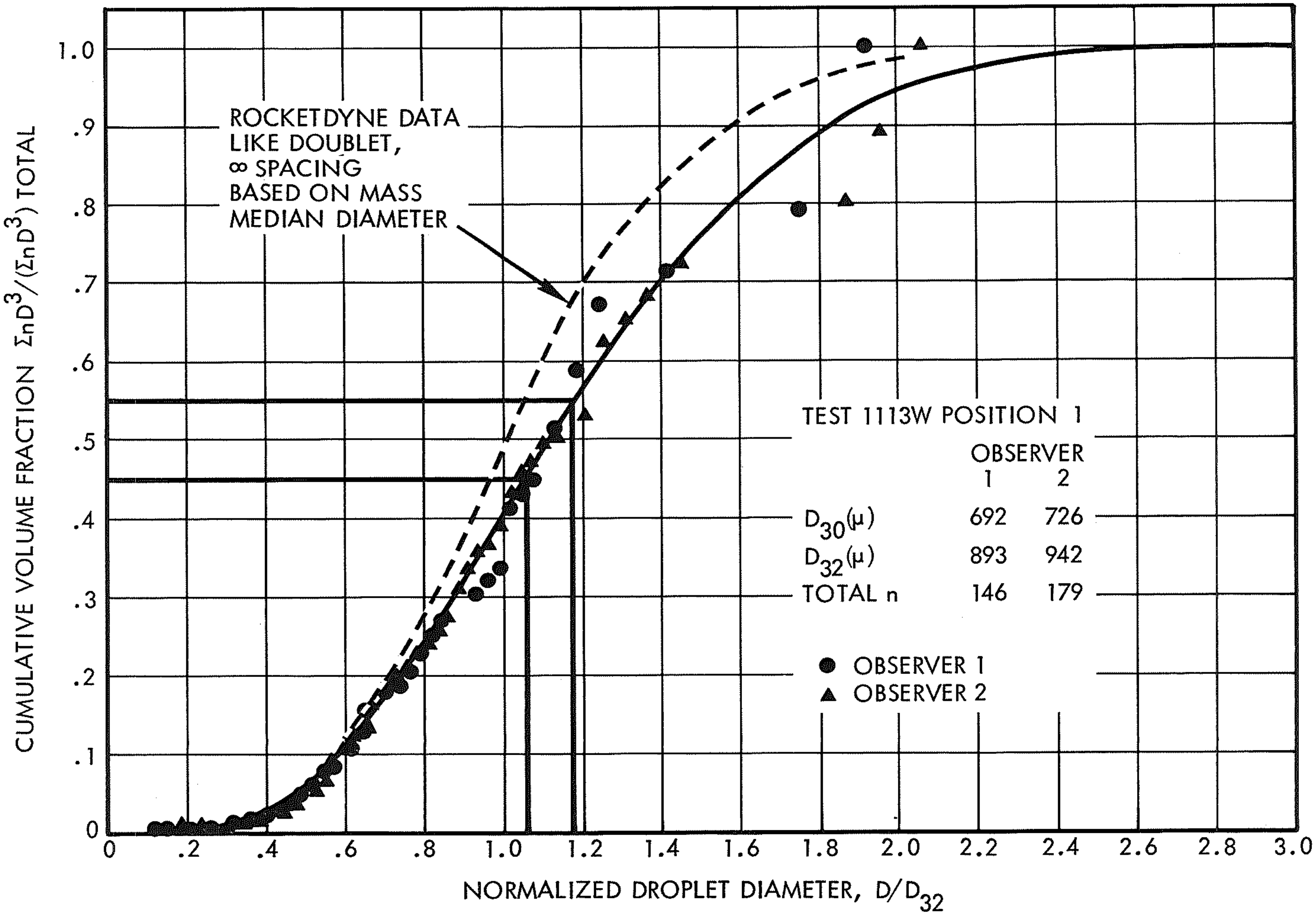

Figure 37. Experimental cumulative volume fraction versus normalized droplet diameter for water flow test B1113W, position 1. Normalized droplets of 1.06 and 1.18 are indicated for 45th and 55th percentiles.

4. CONCLUSIONS

The JPL 45-degree transmission holocamera is a unique tool for the recording of liquid injection and combustion phenomena over distances up to 3 feet (maximum depth of field for the apparatus). Using reconstruction methods developed during this program, the holocamera was shown to have a resolution capability (to 25 microns) commensurate with the general area of interest for the study of reacting sprays. In addition, photographically copied images of reconstructed reacting sprays were amenable to data reduction. Droplet images could be measured and counted. Droplet sizing did, however, require a considerable amount of judgement. This was due to the fact that reacting droplets were predominately non-spherical in geometry and their boundaries were usually not precisely defined. In this regard, the open flame combusting sprays could be consistently characterized as having a "lacy-like" structure or appearance. It should be noted that no distinction between the oxidizer and fuel constituents of the reacting sprays could be made.

Analysis of the open flame reacting spray droplet data showed that reasonable correlations and comparisons could be made with 1) reduced holographic data from a cold flow water spray produced by the same injector element used for the open flame tests and, 2) empirical data generated by other investigators examining the droplet spray characteristics of similar injector elements. Reduction of reacting spray droplet data in a combustion chamber proved to be a more difficult task and indeed, none of the 3-inch-diameter combustion chamber holograms from the previous JPL program proved adequate. Hologram quality was inferior to the open flame recordings due to 1) erosion of the acrylic combustion chambers and, 2) the intense concentration of laser light through a small portion of the chamber which produced a so-called "bright sun" effect in the reconstructed holograms thus obscuring some of the combustion detail.* To a lesser extent, the heavy-wall tubular acrylic chambers produced distorted images at the periphery of the combustion volume.

---

*Concentration of the ruby laser illumination in a comparatively small area of the chamber was done to overcome blockage of the scene light by erosion of the acrylic chambers.

Distortion free viewing of events within combustion chamber reconstructions was limited to the central one-third of the volume.

Limited data reduction of combustion phenomena in a chamber was accomplished, however, using a hologram recorded during an Air Force-sponsored research program. Although the droplet data sample was small, it did demonstrate that quantitative information could be acquired from a hologram of combustion in a thrust chamber operating at approximately 11 atmospheres of pressure. Further, measured drop size information from the combustion chamber hologram recording was compared with a steady-state, one-dimensional vaporization rate-limited combustion mode. The results of the combustion model tend to support the drop size distribution obtained from the hologram.

5. RECOMMENDATIONS

Based upon the results of this and the preceding JPL reacting spray holography program, it is recommended that additional work be conducted to further explore and refine the basic transmission holography techniques for recording reacting sprays. A limited amount of fundamental research should be accomplished in an attempt to separately identify the oxidizer and fuel constituents of bipropellant droplet spray. This work should include the holography of isolated fuel droplets in a gaseous oxidizer and vice versa. Multiple color pulsed laser (red and ultraviolet) holography and direct laser illuminated photography of individual fuel and oxidizer droplets should also be considered as a further means of differentiating between the propellants.

Additional study of the phenomena occurring at or near the impingement point of impinging stream injectors is recommended. Work should start with small scale impinging streams of reactive and non-reactive constituents to develop the necessary holographic techniques required to obtain greater laser light penetration in this critical region of the combustion process.

The data correlations obtained during the present work, in conjunction with the combustion modeling approach, showed excellent promise for the overall technique. Additional effort involving systematic single element size and geometry variations, along with selected multiple elements, is recommended to obtain improved combustion modeling correlation.

To date, holography of burning liquid rocket propellants has been limited to the study of only two earth storable propellant combinations. Additional combustion studies should be made to determine the applicability of holography methods to other propellants. In any event, further holography studies of combustion should be aligned with parallel theoretical modeling of the combustion process so that the combustion models may be verified and refined.

One of the most important aspects of applying holography to the study of distributed phenomena such as reacting sprays is that of acquiring and reducing data. The extremely large amounts of information which can be recorded on a single holographic plate make the task of manually reducing this data a costly and time consuming job. Although some effort has been made along these lines, much work remains. Ideally, one would like to interrogate the real image of the reconstructed hologram using a three-axis scanning device and short working distance magnifiers. To obtain greatest resolution, it is necessary to use ruby radiation from a continuous source such as the Siemens laser. This approach, coupled with a sensing device (to prevent eye damage) and a suitable computer program, offers the next step in sophistication for acquiring and reducing droplet data.

NOMENCLATURE

D_{32}	Sauter mean droplet diameter = $\Sigma n_i D_i^3 / \Sigma n_i D_i^2$, microns
D_{30}	Volume mean diameter = $(\Sigma n_i D_i^3 / \Sigma n_i^{1/3}$, microns
n_i	Number of droplets in droplet diameter interval (25 micron interval used for test data)
D_i	Average equivalent droplet diameter in diameter interval, : i. e., 187. 5 microns in interval from 175 to 199. 99 microns
$\overline{D}$	Mass or volume median diameter = diameter at at $\Sigma n_i^3 / \Sigma n_i D_i^3 / (\Sigma n_i D_i^3)$ Total = 0. 50, microns
D_j, D	Orifice diameter, inches
V_j	Initial jet velocity, ft/sec
V_{air}	Ambient air velocity, ft/sec
μ_L	Liquid viscosity, lb_m/sec-ft
σ_L	Liquid surface tension, dyne/cm
ρ_L	Liquid density, lb/ft^3
θ	One-half of included angle of doublet injection element, degrees
X	D_i/D_{32}
U, C, B, A	Constants
σ	Standard deviation

Subscripts

o	Oxidizer
f	Fuel

REFERENCES

1. R. F. Wuerker, B. J. Matthews and R. A. Briones, "Producing Holograms of Reacting Sprays in Liquid Rocket Engines," Final Report under JPL Contract No. 952023, TRW Systems Report No. 68.4712-024, July 1968.

2. R. F. Wuerker and B. J. Matthews, "Laser Applications—Holography," 5th ICRPG Combustion Conference, CPIA Publication No. 183, December 1968, pp.9-16.

3. R. S. Rogero, B. J. Matthews and R. F. Wuerker, "Pulsed Laser Holography—New Instrumentation for Use in the Investigation of Liquid Rocket Combustion," Proceedings of the 15th International ISA Aerospace Instrumentation Synposium, Vol. 15, May 1969, pp. 1-9.

4. R. F. Wuerker and B. J. Matthews, "Holography of Liquid Rocket Engine Combustion," Liquid Propellant Rocket Combustion Instability, ICRPG Reference Book, D. T. Harrje, Ed., U.S. Govt. Printing Office, Washington D. C. (To be published in early 1970).

5. B. J. Matthews, R. F. Wuerker and D. T. Harrje, "Small Droplet Measuring Technique, Final Report AFRPL-TR-68-156, July 1968. (pp. 52-54 describe resolution theory and testing and in particular, conversion of resolution target readings of lines per millimeter to equivalent particle size in microns).

6. D. A. Gary, "A Study of Injector Spray Characteristics in a Simulated Rocket Combustion Chamber Including Longitudinal Mode Pressure Oscillations," Technical Report No. 730, Department of Aerospace and Mechanical Sciences, Princeton University, June 1966.

7. R. F. Wuerker and B. J. Matthews, "Laser Holocamera Droplet Measuring Device," Final Report AFRPL-TR-69-204, November 1969.

8. R. D. Ingebo, "Drop Size Distributions for Impinging-Jet Breakup in Airstreams Simulating the Velocity Conditions in Rocket Combustors," NACA TN 4222, March 1958.

9. R. Dickerson, K. Tate and N. Barsic, "Correlation of Spray Injector Parameters with Rocket Engine Performance," Technical Report AFRPL-TR-68-147, June 1968.

10. N. Dombrowski and P. Hooper, "A Study of the Sprays Formed by Impinging Jets in Laminar and Turbulent Flow," Journal of Fluid Mechanics, Volume 18, Part 3, March 1964.

REFERENCES (Continued)

11. J. H. Rupe, "A Correlation Between the Dynamic Properties of a Pair of Impinging Streams and the Uniformity of Mixture Ratio Distribution in the Resulting Spray," JPL Progress Report No. 20-209, March 28, 1956.

12. A. Putnam, et al, "Injection and Combustion of Liquid Fuels," WADC Technical Report 56-344, March 1957.

13. B. P. Breen, et al, "Injection and Combustion of Hypergolic Propellants," Dynamic Science, AFRPL-TR-69-48, April 1969.

Appendix A

USAF 1951 RESOLVING POWER TEST TARGET

The resolution of an optical instrument is basically its capacity for imaging fine detail. Stated another way, resolution is concerned with the ability to measure differences based upon the comparison of two very close sources of light. Ultimate resolution is the measure of the closest distance two points of light can be placed and still be recognized as being individual points.

The linear resolution for an optical system may be numerically expressed in terms of lines per millimeter. Resolution devices or targets for evaluating optical systems often consist of geometric patterns which may be "read" or interpreted. A commonly accepted patterned target is the U.S.Air Force 1951 Resolving Power Test Target, which is defined by Military Standard 150-A. This resolution target, shown in Figure A-1, consists of an array of three-line "patterns." The width of a line is equal to the width of the spacing between lines in each pattern. Further, the length of each line is five times its width.

A grouping of two patterns set at right angles to each other is termed an "element" of the test target. The elements are arranged in increasingly smaller sizes. These elemental size changes in the USAF 1951 Target are defined by a geometric progression based upon the sixth root of 2, or $\sqrt[6]{2}$. Stated another way, the number of lines per millimeter doubles every sixth target element.

The target elements are arranged in columnar form. Each column is numbered (from -2 to 7) and each element within a given column is identified by another number (1 to 6). Therefore, an element on the target is described by a column number and a "row" number. The accompanying table (see Figure A-1) provides a listing of the number of lines per millimeter for each element. For the 1951 target, the largest element corresponds to 0.250 lines per millimeter while the smallest is 228 lines per millimeter.

In reading a resolution chart, one identifies the smallest element in which the three-line pattern can be distinguished. The column and row numbers of this element (for example, column 3, row 1 or 3-1) are noted and the corresponding number of lines per millimeter for the element is then conveniently obtained from the Table in Figure A-1. For element 3-1, the value is 8.00 lines per millimeter.

It is also possible to assign an equivalent particle width (or diameter) from the resolution target. Remembering that the width of each line and adjacent space are equal, and taking the reciprocal of the measured resolution in lines per millimeter, the period of the line spacing is obtained (millimeters per line). One-half of the period then, is the smallest object which may be discerned. Thus, if a USAF 1951 target can be "read" to column 3, row 1, the line spacing is 8 lines per millimeter. This is equivalent to 1/8 = 0.125 millimeters per line. One-half of this value is 0.0625 millimeters (width of the line only) or 0.0625 millimeters x 1000 microns per millimeter = 62.5 microns. This would be the smallest width or diameter of an object which could be individually identified by the optical system in question.

Element No. (Row No.)	Group Number (Column Number)									
	-2	-1	0	1	2	3	4	5	6	7
1	0.250	0.500	1.000	2.00	4.00	8.00	16.0	32.0	64.0	128.
2	0.280	0.561	1.12	2.24	4.49	8.98	17.95	36.0	71.8	144.
3	0.315	0.630	1.26	2.52	5.04	10.1	20.16	40.3	80.6	161.
4	0.353	0.707	1.41	2.83	5.66	11.3	22.62	45.3	90.5	181.
5	0.397	0.793	1.59	3.17	6.35	12.7	25.39	50.8	102.	203.
6	0.445	0.891	1.78	3.56	7.13	14.3	28.51	57.0	114.	228.

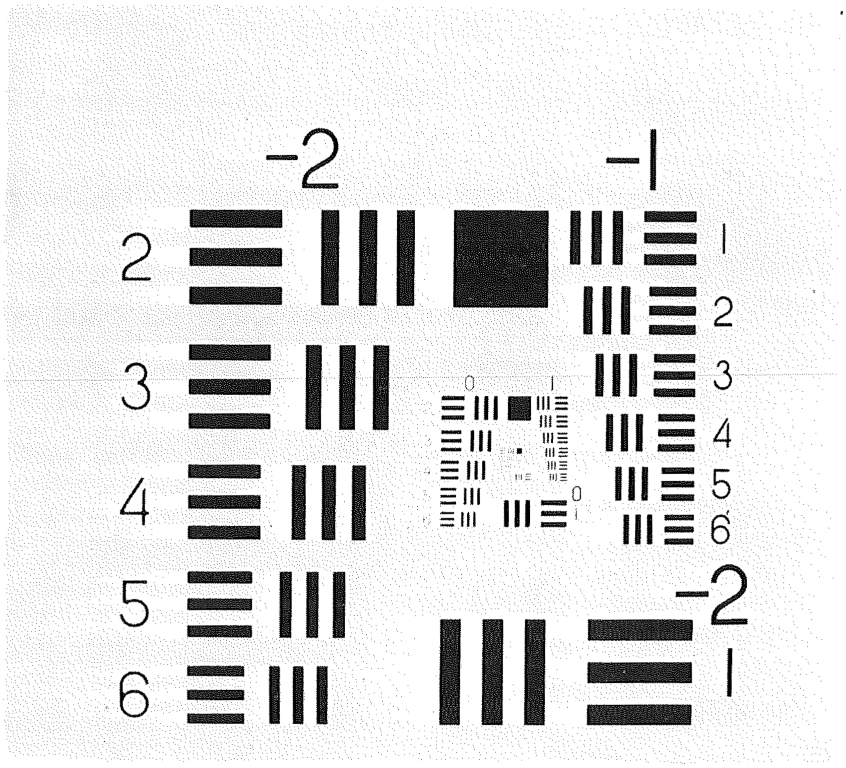

Figure A-1. Photograph of a USAF 1951 Resolving Power Test Target. The table above the photograph indicates the number of lines per millimeter for each element on the target.